

1 **Chemically speciated mass size distribution, particle density, shape and origin of**
2 **non-refractory PM₁ measured at a rural background site in Central Europe**

3 Petra Pokorná¹, Naděžda Zíková¹, Petr Vodička¹, Radek Lhotka^{1,2}, Saliou Mbengue³, Adéla
4 Holubová Šmejkalová⁴, Véronique Riffault⁵, Jakub Ondráček¹, Jaroslav Schwarz¹, Vladimír
5 Ždímal¹

6 ¹Department of Aerosol Chemistry and Physics, Institute of Chemical Process Fundamentals,
7 Czech Academy of Sciences, Rozvojová 135/1, 165 02 Prague, Czech Republic

8 ²Institute for Environmental Studies, Faculty of Science, Charles University, Benátská 2, 128
9 01 Prague 2, Czech Republic

10 ³Global Change Research Institute, Czech Academy of Sciences, Bělidla 986/4a, 603 00
11 Brno, Czech Republic

12 ⁴Czech Hydrometeorological Institute, Air Quality Division, Na Šabatce 2050/17, 143 06
13 Prague, Czech Republic

14 ⁵IMT Lille Douai, Institut Mines-Télécom, Université de Lille, Centre for Energy and
15 Environment, F-59000 Lille, France

16 *Correspondence to: Petra Pokorná (pokornap@icpf.cas.cz)*

17

18 **Abstract**

19 Seasonal variability of non-refractory PM₁ (NR-PM₁) was studied at a rural background site
20 (National Atmospheric Observatory Košetice – NAOK) in the Czech Republic to investigate
21 the effect of regional and long-range atmospheric transport in Central Europe. NR-PM₁
22 measurements were performed by compact time-of-flight aerosol mass spectrometry (C-ToF-
23 AMS), and the chemically speciated mass size distributions, density, shape and origin were
24 discussed. Average PM₁ concentrations, calculated as the sum of the NR-PM₁ (after collection
25 efficiency corrections – CE corrections of 0.4 and 0.33 in summer and winter, respectively) and
26 the equivalent black carbon (eBC) concentrations measured by an aethalometer (AE), were 8.58
27 ± 3.70 μg m⁻³ in summer and 10.08±8.04 μg m⁻³ in winter. Organics were dominant during both
28 campaigns (summer/winter: 4.97 ± 2.92/4.55± 4.40 μg m⁻³), followed by SO₄²⁻ in summer (1.68
29 ± 0.81/1.36± 1.38 μg m⁻³) and NO₃⁻ in winter (0.67 ± 0.38/2.03 ± 1.71 μg m⁻³). The
30 accumulation mode dominated the average mass size distribution during both seasons, with
31 larger particles of all species measured in winter (mode diameters: Org: 334/413 nm, NO₃⁻:
32 377/501 nm, SO₄²⁻: 400/547 nm, and NH₄⁺: 489/515 nm) indicating regional and long-range
33 transport. However, since the winter aerosols were less oxidized than the summer aerosols
34 (comparing fragments f₄₄ and f₄₃), the importance of local sources in the cold part of the year
35 was still enough to be considered. Although aged continental air masses from the south-east
36 (SE) were rare in summer (7%), they were related to the highest concentrations of PM₁, eBC
37 and all NR-PM₁ species, especially SO₄²⁻ and NH₄⁺. In winter, slow continental air masses from
38 the south-west (SW) (44%) were linked to inversion conditions over Central Europe and were
39 associated with the highest concentrations among all NR-PM₁ species as well as PM₁ and eBC.
40 Average PM₁ material density (ρ_m) corresponded to higher inorganic contents in both seasons
41 (summer: ~1.30 g cm⁻³ and winter: ~1.40 g cm⁻³). During episodes of higher mass

42 concentrations ρ_m ranged from 1.30 – 1.40 g cm⁻³ in summer and from 1.30 – 1.50 g cm⁻³ in
43 winter. The dynamic shape factors (χ) decreased slightly with particle mobility diameter (D_m)
44 in both seasons. This study provides insights into the seasonal effects and air mass variability
45 on aerosol particles, focusing on episodes of high mass and number concentrations measured
46 at Central European rural background site.

47

48 **1. Introduction**

49 Studies on airborne particulate matter (PM) are needed to better understand its temporal and
50 spatial variations, atmospheric processing, long-term trends, adverse health effects and
51 environmental consequences, and pollution sources (Putaud, et al., 2004; Tørseth et al., 2012;
52 Belis et al., 2013; EEA 2019). Therefore, detailed analysis of the physicochemical properties
53 of aerosol particles is crucial to understand their processes and lifetime in the atmosphere.
54 Aerosol particles can be characterized by many different properties such number concentration,
55 mass concentration, particle size, mass, volume, density, shape etc. Particle density and shape
56 is an important physical property of atmospheric particles and along with chemical composition
57 is linked to particle emission sources and atmospheric physical and chemical ageing processes.

58 A network of measurement sites as the Aerosol, Clouds, and Trace Gases Research
59 Infrastructure Network (ACTRIS, <https://www.actris.eu/>, last access: February 2022) enables
60 the study of long-term variability of aerosol particle properties in the European environment.
61 However, a prevalent coarse time and size resolution of the measurements still limits our
62 knowledge on the physicochemical properties of aerosol particles (Putaud et al., 2004; 2010;
63 Cavalli et al., 2016). Nowadays, online methods with high temporal resolutions (30 min and
64 less) are available, as aerosol mass spectrometers (AMSs) utilized can quantitatively measure
65 chemical composition as well as the chemically resolved size distributions of submicron non-
66 refractory PM (NR-PM₁) (Jayne et al., 2000; Jimenez et al., 2003a). Although measuring the
67 seasonal variability of NR-PM₁ is becoming more common (Bressi et al., 2021), systematic
68 studies considering chemically speciated mass size distributions are still rare. The available
69 studies have also focused on new particle formation and growth, temporal variations, and the
70 origin and sources of particles, including results presented from urban (Drewnick et al., 2004;
71 Dall'Osto et al., 2009; Hersey et al., 2011; Freutel et al., 2013; Salimi et al., 2015; Kubelová et
72 al., 2015), forestry (Allan et al., 2006), mid-altitude (Freney et al. 2011) and rural (Poulain et
73 al., 2011; Milic et al., 2017) background environments.

74 Measurements at rural background sites representative of wider areas are important to study the
75 influence of regional and long-range transport as well as the long-term trends in PM
76 characteristics. In the Czech Republic, the National Atmospheric Observatory Košetice
77 (NAOK), officially classified as a Central European rural background site, participates in the
78 European Monitoring and Evaluation Programme (EMEP), Aerosol, Clouds, and Trace Gases
79 Research Infrastructure Network (ACTRIS), and Global Atmosphere Watch (GAW) network.
80 This site has been characterized in terms of the local PM_{2.5} chemical composition and seasonal
81 variability (Schwarz et al., 2016), the PM₁ isotopic composition (Vodička et al., 2019) and the
82 PAH_s bound to PM₁ (Křůmal and Mikuška, 2020). Studies conducted at NAOK have also
83 characterized the long-term trends of atmospheric carbonaceous aerosols (Mbengue et al., 2018,
84 2020) and PM_{2.5} elemental compositions and sources (Pokorná et al., 2018). The particle
85 number size distribution (PNSD) and influence of in-cloud and below-cloud scavenging have

86 been investigated with long-term measurements by Zíková and Ždímal (2013, 2016). However,
87 detailed work focused on the seasonal variability in PM chemical composition data with high
88 temporal and spatial resolutions is still lacking at this site. In this paper we assess NR-PM₁
89 based on the chemically speciated mass size distribution, particle density, shape and origin
90 during intensive campaigns in summer and winter. The focus of this study was to characterise
91 individual episodes of high mass and number concentrations determined based on highly-time
92 resolved measurement linked to different air mass types, thereby offering insights into the
93 physicochemical properties and sources of aerosol particles arriving at a rural background site.

94

95 **2. Materials and methods**

96 **2.1 Instrumentation**

97 Two intensive sampling campaigns were carried out in July 2019 (1.7. – 31.7.) and in January-
98 February 2020 (16.1. – 10.2.) at NAOK. During the campaigns, several physical and chemical
99 atmospheric aerosol properties were measured together with complete meteorological data
100 collected from a professional meteorological station (WMO station 11628).

101 The size-resolved NR-PM₁ chemical composition (the sum of organic, sulphate, nitrate,
102 ammonium and chloride) was measured by a compact time-of-flight aerosol mass spectrometer
103 (C-ToF-AMS, Aerodyne, USA, Drewnick et al., 2005) with a 5-min temporal resolution. The
104 instrument was connected to an inlet consisting of a PM_{2.5} sampling head (16.7 l min⁻¹) and a
105 Nafion dryer (Perma Pure MD-110-24P-4). Isokinetic sub-sampling was used to split the flow
106 into AMS (0.1 l min⁻¹) from the main flow. The AMS size and flow as well as ionization
107 efficiency (IE) calibrations in the brute-force single-particle mode (BFSP, Drewnick et al.,
108 2005, monodisperse 350-nm ammonium nitrate aerosol particles) were performed in the
109 beginning, during and after each campaign. The resulting IE was the average IE from all
110 calibrations. Additionally, the measurements were performed with a HEPA filter applied to the
111 inlet to account for zero-value measurements and to adjust the fragmentation table (Allan et al.,
112 2004).

113 Additionally, 12-h PM₁ filter samples were collected by a sequential Leckel Low Volume
114 Sampler (LVS-3, Sven Leckel Ingenieurbüro, Germany) for subsequent chemical analyses of
115 cations, anions and monosaccharide anhydrides (levoglucosan, mannosan and galactosan) using
116 ion chromatography (Dionex ICS-5000+ system, Sunnyvale, CA, USA). More details about the
117 methods can be found in Kozáková et al., 2019.

118 The particle number concentration (PNC) and particle number size distribution (PNSD) were
119 measured every 5 min by a mobility particle size spectrometer (MPSS, IFT TROPOS, Germany,
120 with CPC 3772, TSI USA) in the size range of 10 – 800 nm (a detailed description of the
121 measurement set-up can be found in Zíková and Ždímal, 2013). The cumulative particle number
122 concentrations over seven size ranges (10 – 25 nm, 25 – 50 nm, 50 – 80 nm, 80 – 150 nm, 150
123 – 300 nm, 300 – 800 nm, and 10 – 800 nm) were subsequently calculated from the PNSD.
124 Additionally, the 1-h PM_{2.5} mass concentrations were measured using a beta-gauge (MP101M,
125 Environement SA, France).

126 The concentrations of equivalent black carbon (eBC) were estimated using a 7-wavelength
127 aethalometer (Model AE33, Magee Scientific, Berkeley, CA, USA) sampling through a PM₁₀
128 sampling head (Leckel GmbH) with a 1-min temporal resolution. Additionally, 4-h PM_{2.5} online

129 organic and elemental carbon (OC/EC) concentrations (Sunset Laboratory Inc., USA) were
130 measured following the shortened EUSAAR2 protocol (Cavalli et al., 2010).

131

132 **2.2 Data analysis**

133 The standard data processing procedure of AMS data (i.e., m/z calibration, baseline subtraction,
134 and air beam correction) was carried out by running the Squirrel v1.62 program in Igor Pro data
135 analysis software (WaveMetrics, Inc.).

136 The statistical data treatment was performed using R version 3.6.1 (R Core Team, 2019) with
137 the ggplot2 (Wickham, 2016) and Openair (Carslaw and Ropkins, 2012) packages.

138 **2.2.1 Collection efficiency determination**

139 To determine the collection efficiency (CE; Drewnick et al., 2005) in the AMS, PM₁ filter
140 sampling with subsequent ion chromatography (IC) analysis was conducted in parallel with the
141 AMS measurements. A comparison between the sulphate concentrations measured by AMS
142 and by IC revealed the better suitability of the CE corrections for summer (CE = 0.40; $y =$
143 $0.99x$, $R^2 = 0.95$) as well as for winter (CE = 0.33; $y = 1.00x$, $R^2 = 0.81$) in comparison to the
144 composition-dependent CE correction (CDCE; Middlebrook et al., 2012) shown in Fig. A1.
145 Therefore, CE correction was applied to the AMS data for both seasons to maintain consistency
146 in the data corrections. Similarly, using the same methodology, seasonal CE corrections
147 (summer CE = 0.29 and winter CE = 0.35) were also successfully applied to AMS data
148 measured at a suburban site in Prague (Kubelová et al., 2015).

149

150 **2.2.2 Particle density and shape factor estimation**

151 The effective density (ρ_{eff}) and material density (ρ_m) was estimated along with the dynamic
152 shape factor inferred from the two densities..

153 DeCarlo et al. (2004) gives three different possible definitions of the effective density
154 estimation: i) from mobility and mass measurements, ii) as a fitted parameter, and iii) from
155 mobility and aerodynamic measurements. Here we proceed from the latter definition with the
156 AMS data representing the mass size distributions based on the vacuum aerodynamic diameter
157 (D_{va}) in the approximate size range of 50 to 800 nm (in Squirrel software extrapolated in range
158 10 – 7000 nm), and MPSS data based on mobility diameter (D_m) representing the $dN/d\log D_p$
159 in the size range from 11.3 to 987 nm. In the MPSS data, the D_m were recalculated to vacuum
160 aerodynamic diameters with the assumption of spherical particles as in DeCarlo et al. (2004):

$$161 \quad D_{va} = \frac{D_m}{\rho_0} \rho, \quad (1)$$

162 where D_m is the mobility diameter, D_{va} is the vacuum aerodynamic diameter, ρ_0 is the water
163 density, and ρ is the total density of particles. The position of the main mode of mass
164 distribution (analysis performed with increment of 0.05 g cm^{-3} , uncertainty of the sizing of
165 MPSS – within 3%, see Wiedensohler et al. 2017 and AMS – within 8%, see Takegawa et al.,
166 2005) was compared between the AMS and MPSS data to estimate the aerosol effective density
167 (ρ_{eff}).

168 The mass concentrations of NR-PM₁ species and eBC were converted to the estimated size-
169 dependent material density (ρ_m) based on the following equation from Salcedo et al. (2006).

170
$$\rho_m = \frac{[Total_{AMS} + eBC]}{\frac{[NO_3^-]}{1.75} + \frac{[SO_4^{2-}] + [NH_4^+]}{1.52} + \frac{[Cl^-]}{1.20} + \frac{[Org]}{1.20} + \frac{[eBC]}{1.77}} \quad (2)$$

171 The densities were assumed to be approximately 1.75 g cm⁻³ for ammonium nitrate, ammonium
172 sulphate, and ammonium bisulphate (Lide, 1991); 1.52 g cm⁻³ for ammonium chloride (Lide,
173 1991); 1.20 g cm⁻³ for organics (Turpin and Lim, 2001); and 1.77 g cm⁻³ for black carbon (Park
174 et al., 2004).

175 From the two densities the Jayne Shape factor (S) proposed by Jayne et al. (2000) was inferred
176 and the dynamic shape factor (χ) assuming near the free molecular regime limit $S \sim 1/\chi^{1/3}$
177 (Jimenez et al., 2003b, c; DeCarlo et al., 2004) was estimated.

178 2.2.3 Cluster analysis

179 For both campaigns, 96-hour backwards trajectories were calculated using the Hybrid Single-
180 Particle Lagrangian Integrated Trajectory (HYSPLIT) model (Rolph et al., 2017) with a 500-m
181 AGL starting position and Global Data Assimilation System (GDAS) Archive Information at a
182 resolution of 1° × 1° as input data. The calculations were initialized every 6 hours for the cluster
183 analysis. For the episodes of high mass concentrations (Section 2.2.4) the trajectory ensemble
184 option with calculation initialized every hour and a total duration of 72 hours was utilized. The
185 trajectories were further clustered using Hysplit4 software based on the total spatial variance.

186 From HYSPLIT, the planetary boundary layer height data was extracted using the vmixing
187 program (https://www.ready.noaa.gov/HYSPLIT_vmixing.php). For the planetary boundary
188 layer height calculations, the 0.25° × 0.25° Global Forecast System (GFS) dataset was used as
189 input data to obtain a 3-hour temporal resolution.

190 2.2.4 Episodes of high mass concentrations

191 To determine episodes of high mass concentrations, a twostep approach was utilized: i) the
192 mass size distributions of nitrate, sulphate and organic were depicted in a colour-coded 3D plot
193 and ii) episodes of high mass concentrations were chosen based on a set of criteria: high mass
194 size distribution of at least one main NR-PM₁ specie corresponding to the season –
195 summer/winter ($NO_3^- \geq 0.5/0.2 \mu\text{g m}^{-3}$, $SO_4^{2-} \geq 1/0.5 \mu\text{g m}^{-3}$, $Org \geq 6/2 \mu\text{g m}^{-3}$); monomodal
196 mass size distribution of all main NR-PM₁ species; duration of the episodes min 1.5 hours. Ten
197 summer (S1 – 10) and thirteen winter (W1 – 13) high mass concentration episodes were
198 selected. Additionally, due to the long duration of episode W6 and bimodal mass size
199 distribution of Org, the episode was split into two sections: W6a (67 hours) and W6b (25.5
200 hours). The episodes were studied in detail from the organic fragments, mass size distribution,
201 particle density (material density – ρ_m and effective density – ρ_{eff}) and dynamic shape factor
202 perspectives.

203

204

205

206

207 3. Results and discussions

208 3.1 Campaign overview

209 The campaigns were characterized by prevailing westerly winds with average wind speeds of
210 $3.2 \pm 1.5 \text{ m s}^{-1}$ in summer and $4.4 \pm 3.1 \text{ m s}^{-1}$ in winter (Fig. A2), average temperatures of 18.5
211 $\pm 4.7 \text{ }^\circ\text{C}$ in summer and $1.4 \pm 3.9 \text{ }^\circ\text{C}$ in winter, and negligible precipitation. The average $\text{PM}_{2.5}$
212 was $10.9 \pm 5.9 \text{ } \mu\text{g m}^{-3}$ in summer and $11.8 \pm 9.9 \text{ } \mu\text{g m}^{-3}$ in winter (2019 average annual $\text{PM}_{2.5}$
213 concentration: $10.1 \text{ } \mu\text{g m}^{-3}$, CHMI, 2019a).

214 Based on the PNSD, in summer, particles in the size range of 25 – 80 nm (N25 – 50 and N50 –
215 80) were predominated, whereas in winter, N80 – 150 were dominant (Table 1). Particles in the
216 size range of 25 – 80 nm, referred to as the Aitken mode, are typical for rural background
217 stations and originate from the ageing of particles generated during new particle formation
218 (NPF) events (Costabile et al., 2009). Based on a 5-year study (2013 – 2017) evaluating PNSDs
219 at NAOK, June and July were classified as the months with the highest NPF event frequencies
220 (38 and 36% of days, respectively, Holubová Šmejkalová et al., 2021). The prevailing
221 accumulation-mode particles in winter were presented in Schwarz et al., 2016, as well as in
222 Zíková and Ždímal (2013). The average PNCs recorded during the two studied seasons were
223 lower than the annual mean total concentration ($6.6 \times 10^3 \text{ cm}^{-3}$, Zíková and Ždímal, 2013).

224 Table 1. Average cumulative particle number concentrations (cm^{-3}) measured by MPSS during
225 the summer and winter campaigns.

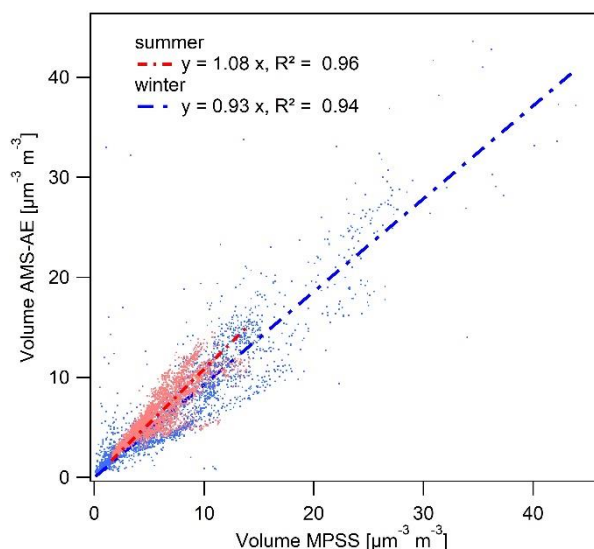
Size range (nm)	Summer	Winter
N10 – 25	979±1488	315±344
N25 – 50	1726±1536	529±402
N50 – 80	1112±715	478±492
N80 – 150	907±472	606±654
N150 – 300	508±191	437±368
N300 – 800	51±41	86±76
N10 – 800 (Total)	4971±2794	2451±1749

226

227 3.2 Volume closure analysis with PNSD

228 For the closure analysis, the total mass concentrations measured by AMS (the sums of the
229 organic, sulphate, nitrate, ammonium and chloride concentrations) were complemented by the
230 eBC mass concentrations. The average PM_1 concentrations for the summer and winter
231 campaigns were $8.58 \pm 3.70 \text{ } \mu\text{g m}^{-3}$ (filter-based 12-hour PM_1 $10.10 \pm 6.44 \text{ } \mu\text{g m}^{-3}$) and $10.08 \pm$
232 $8.04 \text{ } \mu\text{g m}^{-3}$ (filter-based 12-hour PM_1 $11.05 \pm 7.22 \text{ } \mu\text{g m}^{-3}$), respectively. Since the PNSD (10
233 to 800-nm mobility diameter) was measured continuously in parallel with the eBC and NR-
234 PM_1 mass, volume closure of the 10-min averages was performed converting the NR- PM_1 +
235 eBC mass concentrations into volume concentrations using the composition-dependent density.
236 Over the summer campaign, the NR- PM_1 + eBC volume concentrations agreed well with the
237 MPSS volume concentrations (Fig. 1).

238
239
240
241
242
243
244
245
246
247



248 Fig. 1. Comparison between the AMS-AE and MPSS measurements during both campaigns.
249

250 3.3 Concentration and origin of NR-PM₁

251 The CE-corrected mass concentrations of NR-PM₁ species, calculated as functions of time
252 during the two campaigns, are shown in Fig. A3 and the seasonal average concentrations are
253 presented in Table 2. Organics were dominant during both campaigns, followed by SO_4^{2-} in
254 summer and NO_3^- in winter. The PM₁ IC results confirmed higher mean SO_4^{2-} concentrations
255 in summer ($\text{SO}_4^{2-}\text{IC}$ $1.63 \pm 0.84 \mu\text{g m}^{-3}$ and NO_3^-IC $0.23 \pm 0.18 \mu\text{g m}^{-3}$). However, the mean NO_3^-
256 concentrations were slightly lower than the SO_4^{2-} concentrations in winter (NO_3^-IC 0.72 ± 0.52
257 $\mu\text{g m}^{-3}$ and $\text{SO}_4^{2-}\text{IC}$ $0.78 \pm 0.58 \mu\text{g m}^{-3}$). The difference between the NO_3^- concentrations in NR-
258 PM₁ and PM₁ for both seasons could be explained by the loss of ammonium nitrate from the
259 filter due to its dissociation into its gaseous precursors. Good agreement was obtained between
260 the summer average NR-PM₁ NH_4^+ and PM₁ NH_4^+ ($0.80 \pm 0.37 \mu\text{g m}^{-3}$ vs $0.70 \pm 0.36 \mu\text{g m}^{-3}$)
261 in comparison to those obtained in winter ($1.11 \pm 0.99 \mu\text{g m}^{-3}$ vs $0.46 \pm 0.35 \mu\text{g m}^{-3}$). The
262 seasonal variability in nitrate, which displayed higher concentrations in winter, was related to
263 the thermal instability of ammonium nitrate (Seinfeld and Pandis, 2006). A higher share of Cl⁻
264 along with eBC on PM₁ in winter (3 % and 9%, respectively) indicates the influence of coal
265 combustion used for domestic heating (CHMI, 2019b).

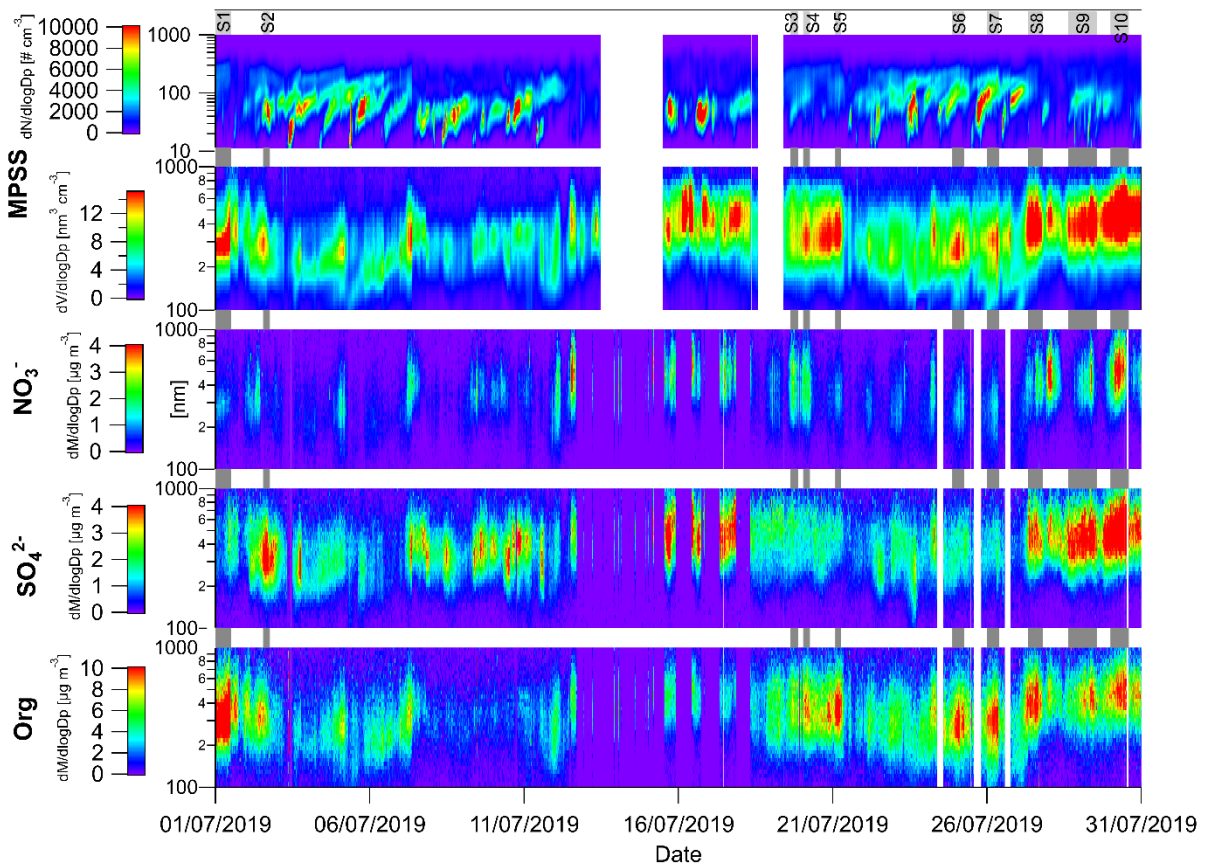
266 Overall, the average SO_4^{2-} concentration obtained in this study was lower than that measured
267 at the Melpitz rural background site ($2.44 \mu\text{g m}^{-3}$ in summer and $1.66 \mu\text{g m}^{-3}$ in winter, Poulain
268 et al., 2011) and lower than the values presented in previous studies by Schwarz et al. (2016)
269 conducted at NAOK (PM_{2.5} IC $2.30 \mu\text{g m}^{-3}$ in summer and $3.86 \mu\text{g m}^{-3}$ in winter) and by
270 Kubelová et al. (2015) conducted in a Prague urban background site ($2.0 \mu\text{g m}^{-3}$ in summer and
271 $4.4 \mu\text{g m}^{-3}$ in winter). The average summer NO_3^- concentration was comparable to those
272 measured in Melpitz ($0.66 \mu\text{g m}^{-3}$), NAOK (PM_{2.5} IC $0.55 \mu\text{g m}^{-3}$) and Prague ($0.80 \mu\text{g m}^{-3}$);
273 however, the winter average concentration was lower than those reported in all three studies
274 (Melpitz: $3.62 \mu\text{g m}^{-3}$, NAOK: $2.83 \mu\text{g m}^{-3}$, Prague: $5.40 \mu\text{g m}^{-3}$). The average organic
275 concentration was lower in summer but higher in winter compared to the values recorded in
276 Melpitz ($6.89 \mu\text{g m}^{-3}$ and $2.08 \mu\text{g m}^{-3}$, respectively). The comparison of organic mass (OM) by

AMS and OC using an OCEC field analyser is shown in Fig. A4. Turpin and Lim, 2001 recommended an OM/OC ratio of 2.1 for non-urban (aged) particles and of 1.6 for urban particles. In this study, the average OM/OC ratio was 2.06 (± 0.68) in summer and 1.51 (± 0.36) in winter. An average OM₁ and OC_{2.5} of 2.1 \pm 1.4 was determined at the Hohenpeissenberg rural site in spring, referring to continental OA (Hock et al., 2002). The higher summer OM/OC ratio could be explained by the presence of more oxidized organic compounds, as the products of photochemical reactions increase the average organic molecular weight per carbon weight (Turpin and Lim, 2001). This result is consistent with the increasing OC/EC ratio observed during summer, when photochemical activity leads to larger secondary organic carbon formation (Mbengue et al., 2018, 2020). Another explanation could be the increased boundary layer height, which enables mixing from higher altitudes and therefore the entrainment of aged, and thus more oxidized, aerosols from long-range transport (Querol et al., 1998). On the other hand, the winter season is characterized by fresh emissions of hydrocarbons owing to the lowered boundary layer height in winter, which does not support the transport of oxidized pollutants within the mixing layer (Schwarz et al., 2008).

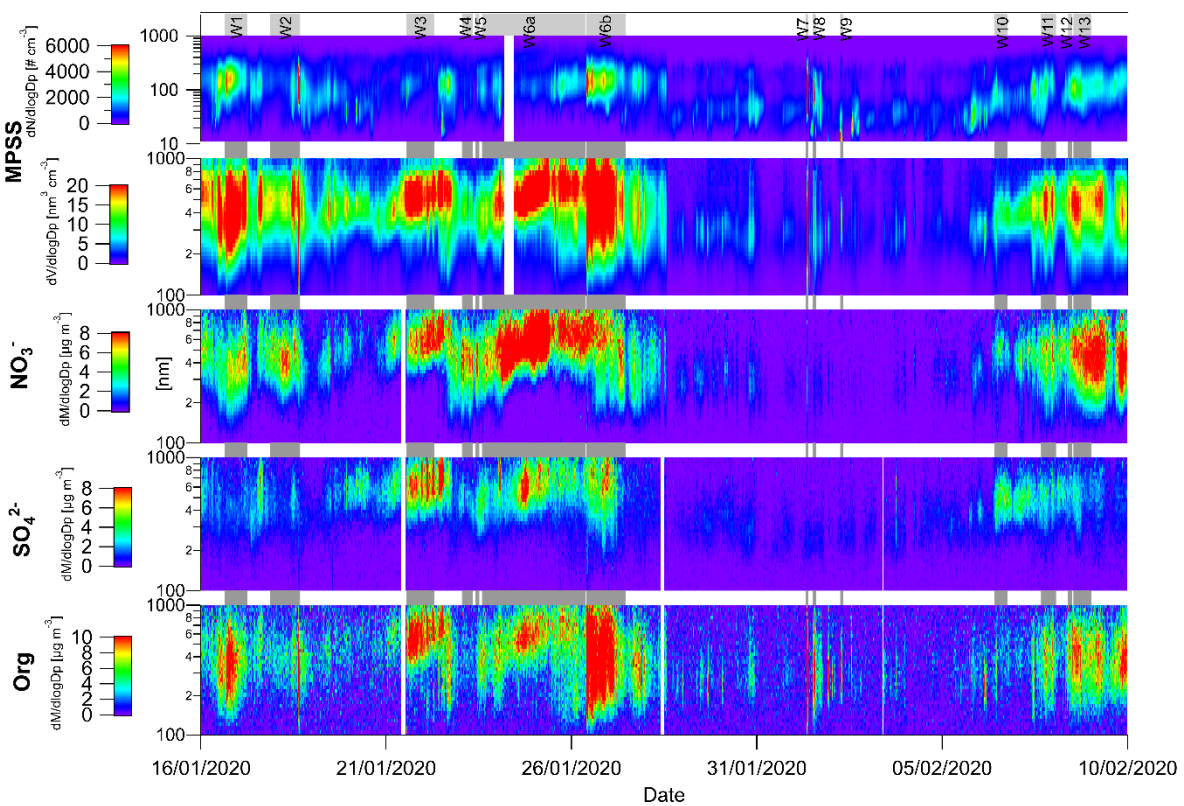
Table 2. Basic statistics of the NR-PM₁ and eBC concentrations (median, mean, standard deviation (SD) and average share of species in the total concentration) measured during summer and winter. The values were calculated from five-min-resolution CE-corrected data.

Summer	<i>Org</i>	SO_4^{2-}	NO_3^-	NH_4^+	Cl^-	<i>eBC</i>
Median ($\mu\text{g m}^{-3}$)	4.32	1.53	0.57	0.75	0.06	0.36
Mean ($\mu\text{g m}^{-3}$)	4.97	1.68	0.67	0.80	0.06	0.40
SD	2.92	0.81	0.38	0.37	0.02	0.20
Average share on PM ₁	56%	21%	8%	10%	1%	4%
Winter						
Median ($\mu\text{g m}^{-3}$)	3.35	0.98	1.67	0.93	0.16	0.84
Mean ($\mu\text{g m}^{-3}$)	4.55	1.36	2.03	1.11	0.18	0.92
SD	4.40	1.38	1.71	0.99	0.09	0.77
Average share on PM ₁	45 %	13 %	20 %	10 %	3 %	9%

Fig. 2 shows the variations in the particle number and volume and in the sulphate, nitrate and organic size distributions as function of time. In summer, several NPF episodes were recorded (Zíková and Ždímal, 2013; Holubová Šmejkalová et al., 2021); however, accumulation-mode particles were prominent in volume and species mass size distributions.



301



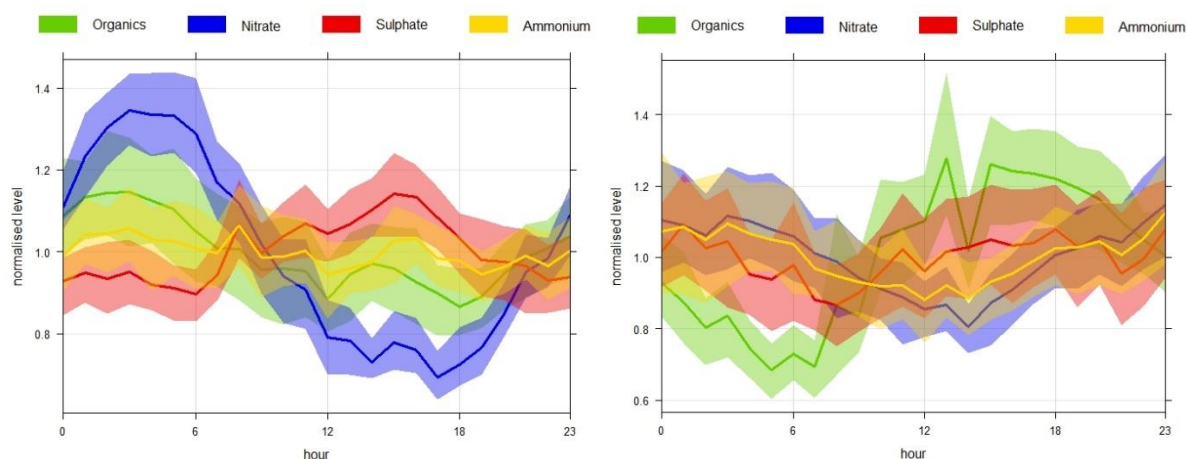
302

303 Fig. 2. Time series of particle number and volume concentrations obtained by MPSS (D_{va}
 304 recalculated from mobility diameter) and mass size distributions of nitrate, sulphate and

305 organics obtained by AMS in summer (top) and in winter (bottom) with marked episodes of
306 higher mass concentrations.

307 The accumulation mode of SO_4^{2-} does not show a large amount of variation, indicating a
308 regional origin. In contrast, NO_3^- shows diurnal variations in mass concentrations
309 corresponding to the local photochemical formation of this species (Fig. 3). In winter, the
310 accumulation mode dominated all distributions and was linked to regional and/or long-range
311 transport (see 3.4 Size distribution of NR-PM₁).

312



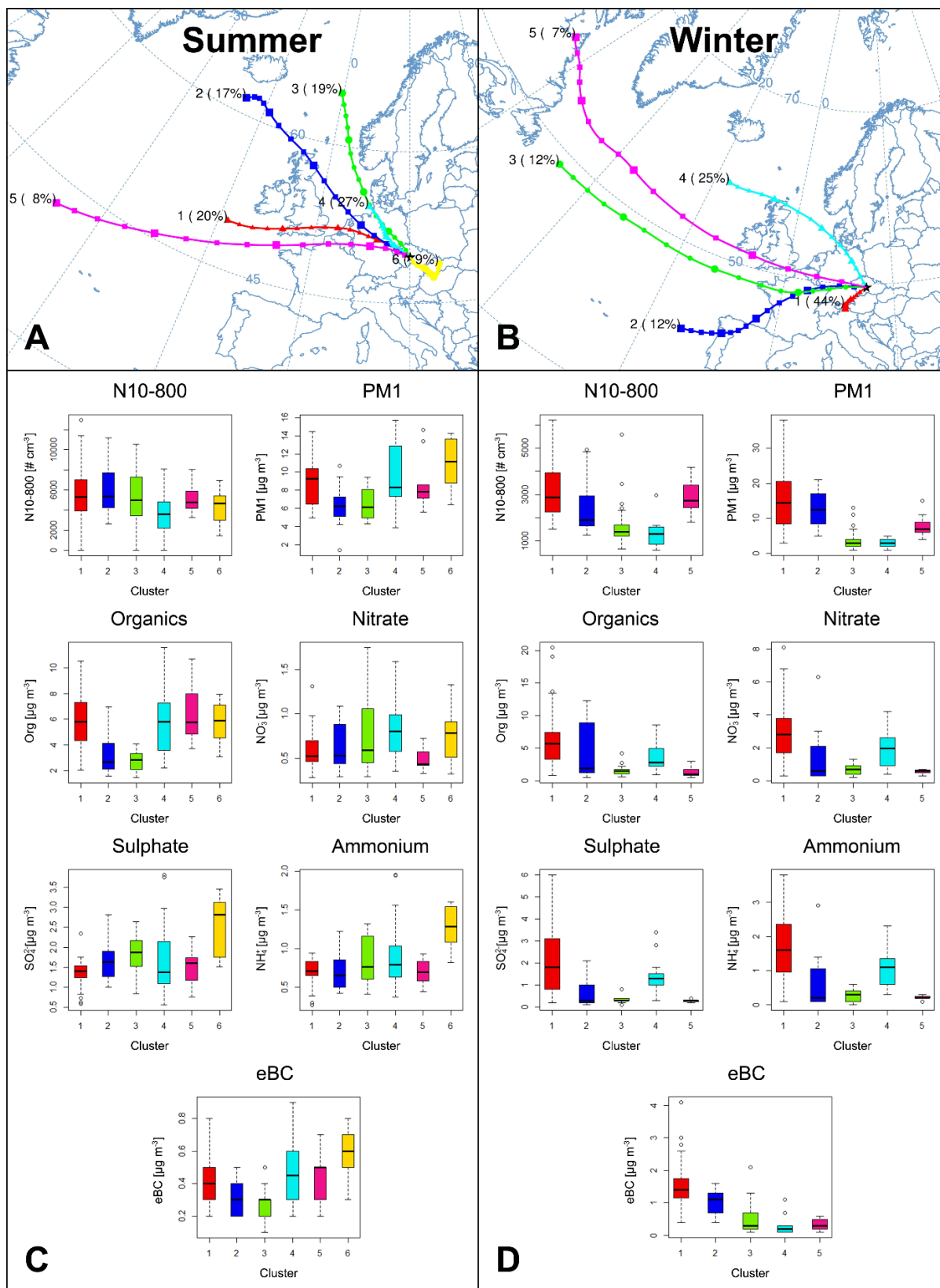
313

314 Fig. 3. Mean diurnal trends (time in UTC) of the NR-PM₁ species (95% confidence interval) in
315 summer (left) and winter (right).

316 To determine the origin of NR-PM₁ species, back-trajectories describing their air mass origins
317 were clustered using the HYSPLIT model into 6 and 5 clusters in summer and winter,
318 respectively (Fig. 4), and linked to the PM₁, N10 – 800, organic, nitrate, sulphate, ammonium
319 and eBC concentrations. A seasonal difference was observed in the air mass back-trajectories,
320 with continental air masses prevailing in summer and marine air masses prevailing in winter.

321 In summer, clusters #1, 2 and 3 (fresh marine air masses from the NW, 56%) and cluster #4
322 (continental air masses from the NW, 27%) were most frequent. Although aged continental air
323 masses from the SE probably related to stable anticyclonic conditions (cluster #6) were rare
324 (7%), they were connected with the highest concentrations of PM₁, eBC and all NR-PM₁ species
325 (Fig. 4). The highest particle number concentrations (N10 – 800) were linked to fresh marine
326 air masses (cluster #1, 2 and 3). There was statistically significant difference among all clusters
327 at the 0.05 level (Kruskal-Wallis test).

328 In winter, slow continental air masses from the SW cluster #1 (44%) prevailed. The air masses
329 remaining over Central Europe, likely under inversion conditions, were associated with the
330 highest concentrations of PM₁, eBC and all NR-PM₁ species. The high pollution loads over
331 Central Europe agree well with the high average mass concentrations of secondary species
332 during periods in which air masses are advected from Central Europe to Paris (Freney et al.,
333 2011, Crippa et al., 2013; Freutel et al., 2013, Freney et al., 2014). N10 – 800 was mainly linked
334 to marine clusters #1 and 5. There was statistically significant difference among all clusters at
335 the 0.05 level.



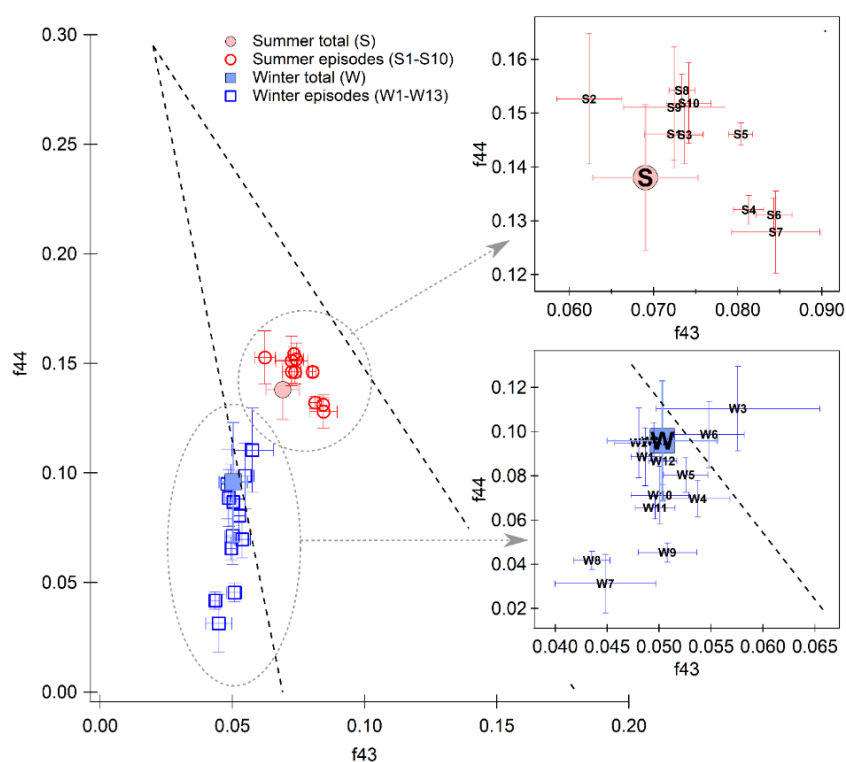
336

337 Fig. 4. Geographical locations of the means of the clusters observed in summer (A) and winter
 338 (B) along with boxplots of the PM₁, N10 – 800, organic, nitrate, sulphate, ammonium and eBC
 339 concentrations in individual clusters measured during the summer (C) and winter (D)
 340 campaigns. The boxes are colour coded as the clusters, the black horizontal line is the median,
 341 the boxes border the 25th and 75th percentiles and the whiskers represent 1.5 x IQR.

342 Based on the mass size distributions of the species (Fig. 2), ten summer (S1 – 10) and 13 winter
 343 (W1 – 13) high mass concentration episodes were selected (Table A1). The organic mass
 344 dominated in summer; however, distinct episodes of high SO_4^{2-} concentrations (S2, S8, S9,
 345 S10) linked to continental air masses from the NW and S-SE were also recorded (Fig. A4). In
 346 winter, episodes of dominant SO_4^{2-} (W10) and NO_3^- (W1, W2, W4, W5, W6) concentrations
 347 were observed. W10 was influenced by marine air masses reaching NAOK over the UK,
 348 Benelux and Germany. The episodes of high NO_3^- concentrations were mainly linked to
 349 continental air masses (from the NW-SW, Fig. A6) from northern France, Benelux, central
 350 Germany and northern Italy. These regions were traced as hotspots of high particulate nitrate
 351 concentrations related to intense agricultural activities under anticyclonic conditions in late-
 352 winter and early-spring (Waked et al., 2014; Petit et al., 2017, 2019; Favez et al., 2021).

353 In summer, the highest Org concentrations ($14.58 \mu\text{g m}^{-3}$) together with the lowest SO_4^{2-} and
 354 NH_4^+ ($1.24 \mu\text{g m}^{-3}$ and $0.91 \mu\text{g m}^{-3}$) concentrations were observed during the S1 night-morning
 355 episode linked to western continental air masses (Table A1 and Fig. A3). S10 represents the
 356 night-morning-early afternoon episode of the highest concentrations of SO_4^{2-} , NO_3^- and NH_4^+
 357 ($6.14 \mu\text{g m}^{-3}$, $3.37 \mu\text{g m}^{-3}$, and $2.98 \mu\text{g m}^{-3}$, respectively) resulting from mixed continental air
 358 masses (NW-S) that were potentially influenced by emissions from coal power plants situated
 359 in North Bohemia.

360



361
 362 Fig. 5. Comparison of organic fragments f_{44} and f_{43} for the whole summer and winter campaigns
 363 (full markers) and for specific episodes (empty markers). Bars represent the standard deviation
 364 and the triangular space area typical for ambient OOAs (Ng et al., 2010).

365 The highest concentrations of Org ($15.63 \mu\text{g m}^{-3}$) as well as low concentrations of SO_4^{2-} , NO_3^-
 366 and NH_4^+ ($0.74 \mu\text{g m}^{-3}$, $0.93 \mu\text{g m}^{-3}$ and $0.96 \mu\text{g m}^{-3}$, respectively) measured in winter during
 367 W7 were influenced by maritime air masses crossing France and Germany before reaching the

368 NAOK (Fig. A6). Nevertheless, a one-day inversion preceded this episode (Fig. A3),
369 characterized by less oxidized OA (Fig. 5, Fig. A7). In contrast, the highest winter SO_4^{2-} and
370 NH_4^+ concentrations ($7.13 \mu\text{g m}^{-3}$ and $7.90 \mu\text{g m}^{-3}$, respectively) measured in the W3 episode
371 and the highest NO_3^- concentrations ($10.66 \mu\text{g m}^{-3}$) measured in the W6a episode were
372 characterized by slightly below-freezing temperatures (average temperature $-2.4^\circ\text{C} \pm 1.3^\circ\text{C}$),
373 which probably arose due to inversion conditions in Central Europe. The conditions prevailing
374 during the W6a episode, in combination with ammonia due to the agricultural activities
375 including the spreading of fertilizers, probably induce increases of particulate nitrate and
376 ammonium concentrations similarly as reported by Favez et al., 2021 for Northern France.

377 Organic fragments f_{44} and f_{43} (ratios of organics in m/z 44 and m/z 43 to total organics) can
378 serve as a proxy of aerosol oxidation and its aging, respectively (Ng et al., 2010). In simplified
379 form, more oxidized aerosols have higher f_{44} and lower f_{43} while less oxidized and more volatile
380 aerosols have the opposite f_{44} vs f_{43} relationship. These oxidation properties of organic aerosols
381 are well defined by the triangular region defined by Ng et al. (2010). This triangular area is
382 shown in Fig. 5 together with the evolution of f_{44} and f_{43} fragments during both campaigns.
383 In general, it shows that winter aerosols were less oxidized than summer aerosols. This results
384 along with the organics diurnal trends of late evening maxima (Fig. 3) and polar plots (Fig. A5)
385 pointing to the importance of local sources during the cold part of the year. The importance of
386 local fossil fuels combustion for residential heating as a source of fresh OA/ hydrogen-like OA
387 in winter is presented in a study by Chen et al., 2021 (under review). In summer, the oxidation
388 rate of organic aerosols within the episodes does not differ greatly, and most of the episodes
389 revealed more oxidized organic aerosols (MO-OOAs) or less volatile organic aerosols (LV-
390 OOAs) (e.g. Jimenez et al. (2009); Crippa et al. (2013)). Within the summer campaign, the most
391 oxidized aerosols were detected during the afternoon episode S2 (Fig. 5), at which time the
392 highest global radiation was also measured (Table A1.). In contrast, S4, S6 and S7 represent
393 night-time and early morning episodes, and S5 represents a night-time and morning episode,
394 and thus less oxidized aerosols (Fig. 5). In winter, the difference between the episodes is more
395 obvious, mainly due to the higher variability in the local sources that influence the receptor site.
396 The W7, W8 and W9 (Fig. 5) episodes are exceptions; these episodes were linked to clean fresh
397 marine air masses that cause prevailing influence of local, fresh, and less oxidized aerosol (Fig.
398 A6.).

399 The organic fragment f_{60} was used as a biomass-burning (BB) marker. If ambient aerosols are
400 characterized by an f_{60} higher than 0.003, they are considered to be influenced by BB emissions
401 (Cubison et al., 2011). During both campaigns, the average f_{60} was 0.003, in contrast to the
402 presence of levoglucosan in the PM_{10} samples during both seasons (summer average 0.02 ± 0.02
403 $\mu\text{g m}^{-3}$ and winter average $0.18 \pm 0.20 \mu\text{g m}^{-3}$). Levoglucosan concentrations point to BB
404 influence, which was similarly discussed in previous studies conducted at NAOK by Schwarz
405 et al. (2016) and Mbengue et al. (2020). Additionally, a comparison of fragments f_{44} and f_{60}
406 enabled us to assess the presence of fresh or aged organic aerosols emitted by BB (e.g., Milic
407 et al., 2017), revealing that aged organic aerosols from BB influenced the site during both
408 seasons, especially in winter (Fig. A7). The comparison of organic fragments f_{44} and f_{60}
409 determined at the rural and urban background sites shows a difference in the ageing of BB
410 emissions with the presence of fresh organic aerosols at the urban site and aged organic aerosols
411 at the rural site in winter (Fig. A8).

412

413

414 3.4 Size distribution of NR-PM₁

415 The average mass size distributions of the main NR-PM₁ species (except chloride) during the
 416 entire summer and winter campaign are presented in Table 3. To determine the mode diameters
 417 and the widths of the size distributions, the mass distributions were fitted with log-normal
 418 modes using the Igor MultiPeak Package as follows:

$$419 \quad y = M \exp \left[- \left(\frac{\ln(x/x_0)}{width} \right)^2 \right], \quad (3)$$

420 where M is the amplitude, x_0 is the peak position in nm, and $width$ denotes the peak width. For
 421 each season, the mean spectra were fitted separately with one peak, and fitting was also
 422 performed for episodes S1-10 and W1-13.

423 The accumulation mode dominated the average mass size distributions during both campaigns,
 424 with larger particles of all species observed in winter (Table 3). Shifts towards larger SO_4^{2-} ,
 425 NO_3^- and NH_4^+ particles in winter compared to summer were also observed in a previous study
 426 by Schwarz et al. (2012) that determined urban aerosol chemical compositions and size
 427 distributions using a 7-stage impactor with an upstream diffusional aerosol drier. The SO_4^{2-}
 428 particles were significantly larger than the NO_3^- particles during both measurement campaigns
 429 except for those collected during two episodes (W7 and W9) with regional transport (Table A1).
 430 An accumulation mode of SO_4^{2-} with regional origin was even detected during a Mexico City
 431 Metropolitan Area field study by Salcedo et al. (2006). Dall'Osto et al. (2009) also observed
 432 two nitrate particle types at an urban background site, both of which were internally mixed with
 433 sulphate, ammonium and carbon: the locally produced particles were smaller than 300 nm,
 434 while the regional particles peaked at 600 nm. In a study by Schwarz et al. (2012) at an urban
 435 site in Prague, two types of SO_4^{2-} particles were determined. SO_4^{2-} particles in sea-influenced
 436 aerosol samples showed maxima between 210 and 330 nm (condensation growth) for both
 437 seasons, and SO_4^{2-} particles in continental-influenced samples showed maxima between 500
 438 and 890 nm in winter and between 330 and 500 nm in summer (droplet-phase growth). NO_3^-
 439 particles with maxima between 330 nm and ~500 nm were observed under maritime and
 440 continental air masses during both seasons. Freutel et al., 2013 observed a single mode of NR-
 441 PM₁ species of approximately 300 nm under marine air masses as well as a shift of the
 442 accumulation mode to a larger size (approximately 400 nm) during a summer campaign in the
 443 Paris region due to aerosol particle ageing of continental air masses from Central Europe.
 444 During a summer measurement campaign in New York, the average mass distributions of NO_3^- ,
 445 SO_4^{2-} and NH_4^+ were monomodal, with mode diameters of 440 nm, 450 nm and 400 nm,
 446 respectively, and the average Org mass distribution was bimodal, with mode diameters of 80
 447 nm and 360 nm (Drewnick et al., 2004). A study by Freney et al. (2011) conducted during three
 448 seasons at the Puy-de-Dôme research station presented a major accumulation mode of NR-PM₁
 449 species peaking at 600 nm, indicating aged aerosol particles.

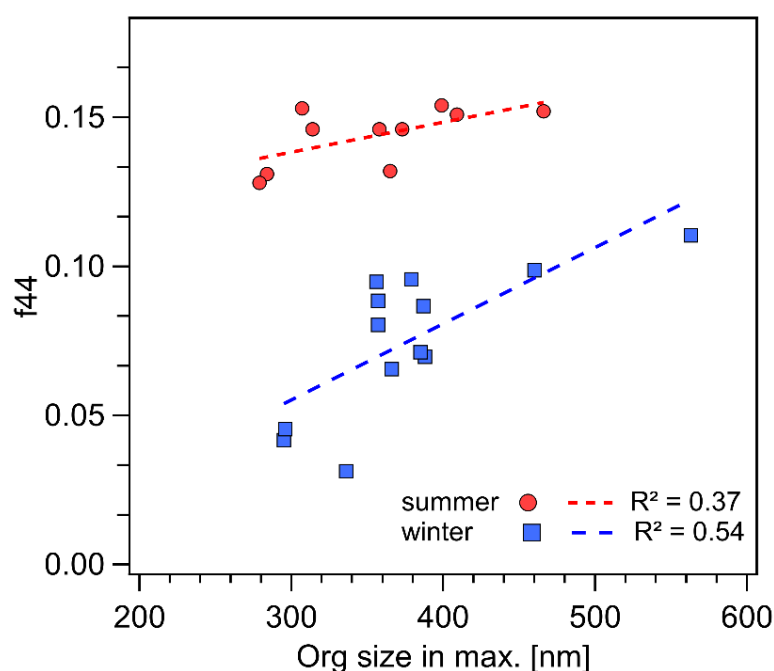
450 Table 3. Mode diameter of mass distributions of species measured by AMS (D_p corresponds to
 451 the vacuum aerodynamic diameter (D_{va})) for the summer (left) and winter (right) campaigns.

	Org	SO_4^{2-}	NO_3^-	NH_4^+
Summer D_{va} (nm)	334	377	401	497
Winter D_{va} (nm)	413	501	547	517

452

453 In summer, the smallest mode diameters of Org (279 nm) and NO_3^- (253 nm) were observed
 454 during the S7 episode, while for SO_4^{2-} and NH_4^+ (325 nm and 335 nm, respectively), they were
 455 influenced by continental air masses of regional origin during the S2 episode (from the N-NE-
 456 E, Fig. A5). In contrast, the largest mode diameters (Org: 466 nm, NO_3^- : 491 nm, SO_4^{2-} : 494
 457 nm and NH_4^+ : 478 nm) were recorded during the S10 episode by continental long-range
 458 transport from the W-NW (Fig. A5). The smallest mode diameters of all species (Org: 295 nm,
 459 NO_3^- : 240 nm, SO_4^{2-} : 242 nm and NH_4^+ : 365 nm) in winter (W8) were linked to fresh marine
 460 air masses, and the largest winter diameters (Org: 563 nm, NO_3^- : 609 nm, SO_4^{2-} : 636 nm and
 461 NH_4^+ : 607 nm, W3) were linked to the regional and long-range transport of air masses of
 462 continental origin and were likely influenced by inversion conditions (Fig. A6). The aging of
 463 aerosol particles is often connected with particle growth similarly as with oxidation of organic
 464 mass. Comparison of fragment f_{44} and mode diameter fully confirmed the ideas. (Fig. 6). In
 465 both seasons, the correlation of the linear fit between Org size and f_{44} was significant (p-value
 466 < 0.001). However, the data presented here does not allow us to extend this size range due to
 467 both instrumental (C-ToF-AMS particle size range is ca from 50 – 800 nm) and data
 468 characterization reasons, as we did not observe a major mode of organics at sizes below 200
 469 nm.

470 In general, however, Fig. 6 suggests that the larger the particles with the organic contribution,
 471 the more oxidised they are due to its longer residence time in the atmosphere. The milder slope
 472 of the line for the summer dataset (Fig. 6) indicates that oxidation is still occurring on the
 473 particles, but appears to be approaching an oxidation limit with growing particle size. In the
 474 case of winter, the steeper slope of the line and lower f_{44} values for smaller particles suggest
 475 that the change of oxidation state with particle size is relatively more intense than in summer
 476 (Fig. 6). However, even so, under the given winter conditions (e.g., lower photochemical
 477 oxidation in winter than in summer), the degree of oxidation of organic aerosols does not reach
 478 the same level as in summer.



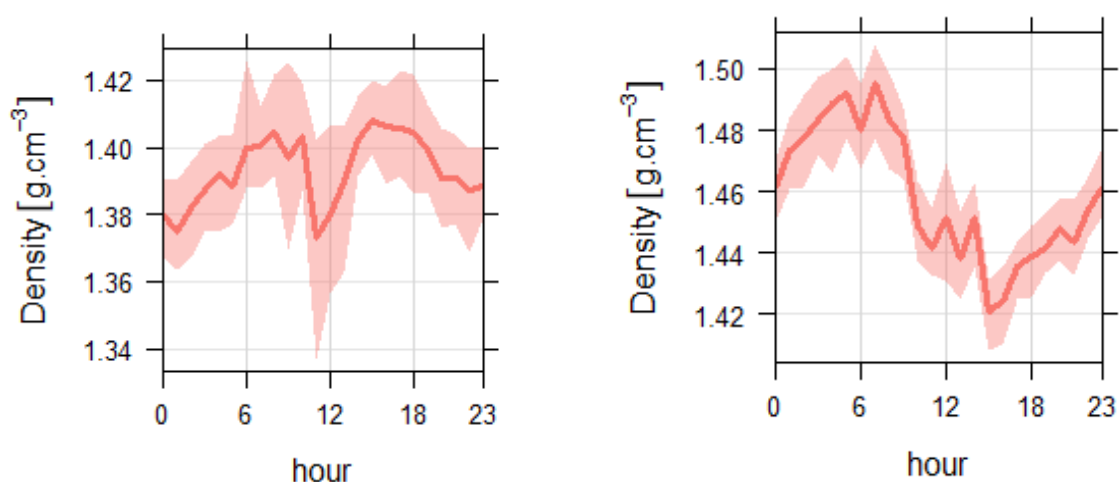
479
 480 Fig. 6. Relationship between the organic fragment f_{44} and the size of the organic fraction during
 481 episodes of high NR-PM₁ species mass concentrations in both seasons.

482

483 3.5 Particle density and shape factor

484 The particle density and shape factors were calculated for each episode of high mass
485 concentrations.

486 The densities (ρ_{eff}) calculated based on the particle mass size distributions using Eq. (1)
487 corresponding to the episodes discussed in section 3.4 (Size distribution of NR-PM₁) and
488 summarised in Table A1 ranged from 1.40 – 1.60 g cm⁻³ in summer and from 1.30 – 1.75 g cm⁻³
489 in winter (Table 4, Fig. A9 and Fig. A10). The densities calculated using Eq. (2) ranged from
490 1.30 to 1.40 g cm⁻³ in summer (with a seasonal average of 1.34 ± 0.28 g cm⁻³) and from 1.30 to
491 1.50 g cm⁻³ in winter (with a seasonal average of 1.44 ± 0.16 g cm⁻³) (Table 4). The average
492 summer density (ρ_m) did not show a diurnal trend compared to the winter density (Fig. 7),
493 followed by a diurnal trend (inverse dependence) observed for organics (Fig. 3). The summer
494 diurnal variation in the concentrations of organics was flatter than that in winter and was not
495 sufficient to significantly affect the diurnal density trend. In summer, we observed the most
496 significant diurnal trend for nitrate, yet the absolute concentrations of nitrate were low, and
497 therefore this variation did not significantly affect the summer diurnal density trend.



498

499 Fig. 7. Diurnal trends of average ρ_m calculated based on Eq. (2) in the main text from Salcedo
500 et al., 2006 in summer (left) and winter (right).

501 In summer, where there was a higher ratio of ammonium sulphate, the density increased. In
502 winter, the density was influenced by the inorganic content (ammonium nitrate and sulphate).
503 In both seasons, the density increased with a decrease in the organic ratio. This relation
504 evidently arises from the parameters in Eq. (2) (Fig. 8). The largest uncertainty in the PM
505 density calculations performed using Eq. (2) is linked to the density of organics, which was set
506 to 1.2 g cm⁻³. The density applied for the organic fraction refers to the urban and urban
507 background stations (Turpin and Lim, 2001), and the organics density of a rural background
508 site is expected to be higher than that of an urban site due to organic aerosol ageing. However,
509 a density of 1.2 g cm⁻³ was also utilized in a study conducted by Freney et al. (2011) at a mid-
510 altitude Puy-de-Dôme site and in a study conducted by Poulain et al. (2020) at a rural
511 background site in Melpitz. To be able to compare our results with above mentioned studies,
512 we also used density of 1.2 g cm⁻³ for organics in Eq. (2). Therefore, as the mass fraction of

513 organics in the aerosols increased, the density calculated using Eq. (2) converged to a value of
 514 1.2 g cm^{-3} (Fig. 8). The use of higher density value for Org in Eq. (2) (e.g., 1.3 and 1.4 g cm^{-3})
 515 affects the overall density value, thus ρ_m is more in agreement with ρ_{eff} . Increasing value of the
 516 Org density in Eq. (2) also flatten the diurnal trend in winter, but it still holds significant diurnal
 517 variations (Fig. A11).

518 Values of Jayne shape factor (S) and the inferred dynamic shape factor (χ) for summer and
 519 winter episodes of high mass concentrations are presented in the Table 4. In summer the
 520 dynamic shape factor was almost constant ($1.02 - 1.09$) and shape of the particle nearly
 521 spherical as a sphere $\chi = 1$ (Hinds, 1999). In winter dynamic shape factor ranged from 0.96 to
 522 1.15 implying particles of nearly spherical shape and/or as compact agglomerates (DeCarlo et
 523 al., 2004; Zelenyuk et al., 2006). There was a slight decrease in dynamic shape factor (χ) with
 524 particle size (Fig. 9, statistically significant at the 0.05 level for winter). In comparison with the
 525 laboratory studies, the dynamic shape factor increased with particle mobility diameter or
 526 remained constant (Jimenez et al., 2003b, c; Slowik et al., 2004; Park et al., 2004; Zelenyuk et
 527 al., 2006). Additionally, in the study by Zelenyuk et al., 2006 the produced organic particles
 528 were found to be nearly spherical and the data suggested that an addition of organics to
 529 ammonium sulphate particles lowers their dynamic shape factor.

530 Table 4. Particle densities (g cm^{-3}) and shape factors calculated during episodes of high mass
 531 concentrations using AMS data in summer (a) and winter (b).

532 a)

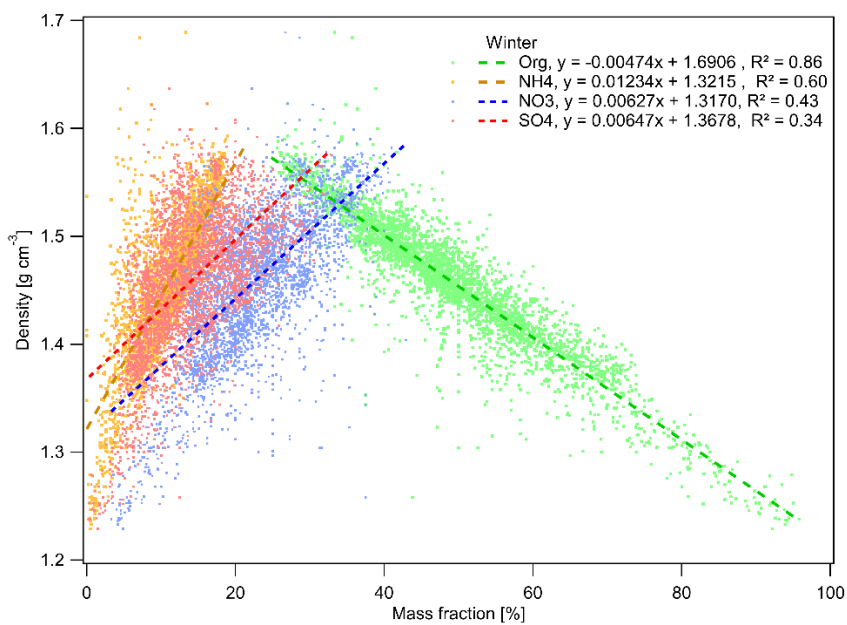
Episode	S1	S2	S3	S4	S5	S6	S7	S8	S9	S10
AMS										
Density (ρ_{eff})	1.45	1.60	1.50	1.55	1.40	1.45	1.45	1.45	1.45	1.50
Density (ρ_m)	1.30	1.40	1.40	1.40	1.30	1.30	1.30	1.35	1.40	1.40
Jayne shape factor (S)	1.12	1.14	1.07	1.11	1.08	1.12	1.12	1.07	1.04	1.07
Dynamic shape factor (χ)	1.08	1.09	1.05	1.07	1.05	1.08	1.08	1.05	1.02	1.05
# of spectra	145	61	73	61	49	109	109	133	265	169

533

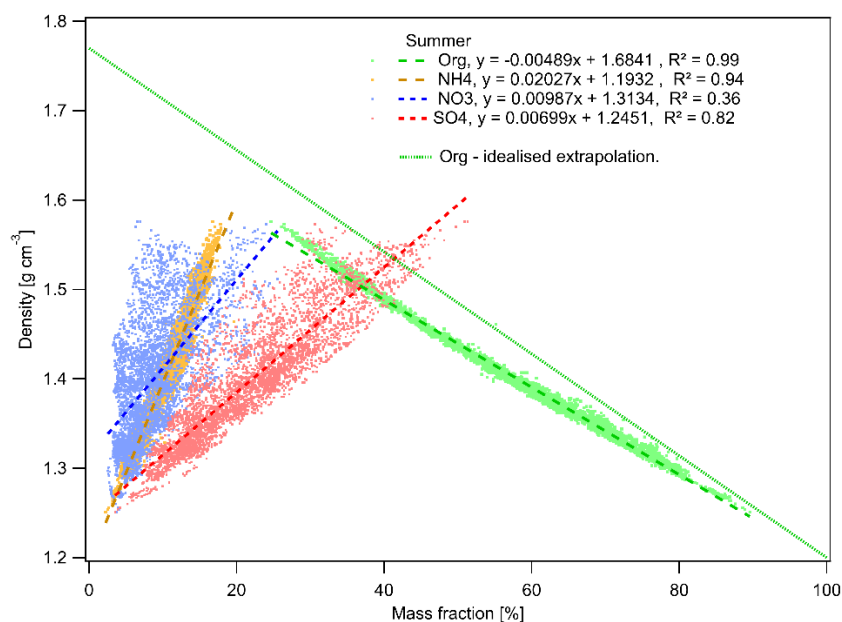
534 b)

Episode	W1	W2	W3	W4	W5	W6a	W6b
AMS							
Density (ρ_{eff})	1.40	1.40	1.70	1.60	1.70	1.6	1.55
Density (ρ_m)	1.40	1.50	1.50	1.50	1.50	1.50	1.40
Jayne shape factor (S)	1.00	0.93	1.13	1.07	1.13	1.07	1.11
Shape factor (χ)	1.00	0.96	1.09	1.04	1.09	1.04	1.07
# of spectra	175	229	337	85	25	805	307
Episode	W7	W8	W9	W10	W11	W12	W13
AMS							
Density (ρ_{eff})	1.55	1.60	1.45	1.75	1.50	1.60	1.55
Density (ρ_m)	1.30	1.30	1.30	1.50	1.40	1.40	1.40
Jayne shape factor (S)	1.19	1.23	1.12	1.17	1.07	1.14	1.11
Dynamic shape factor (χ)	1.12	1.15	1.08	1.11	1.05	1.09	1.07
# of spectra	19	25	19	97	115	31	139

535



536



537

538 Fig. 8. The relationship between density (ρ_m), calculated according to Eq. 2, and mass fractions
 539 of the main NR-PM₁ species. Idealized extrapolation of organics densities is added to the
 540 summer figure for $\rho = 1.2 \text{ g cm}^{-3}$ at 100% Org, and $\rho = 1.77 \text{ g cm}^{-3}$ for 0% organics.

567 during the winter months, and Qiao et al. (2018) reported a decrease in particle effective
 568 densities ranging from 1.43 to 1.55 g cm⁻³ at rural sites (Changping, China) with increasing
 569 particle sizes. The dynamic shape factor was almost constant (1.00 – 1.05) and shape of the
 570 particle spherical, except the episode N_W1 (1.15) with particles of nearly spherical shape
 571 and/or as compact agglomerates.

572 Table 5. Particle effective densities (g cm⁻³) and shape factors calculated during episodes of
 573 high particle contributions to N10 – 800 using MPSS data.

Episode MPSS	N_W1	N_W2	N_W3	N_W4	N_W5	N_W6	N_W7	N_W8
Density (ρ_{eff})	1.85	1.45	1.50	1.55	1.45	1.55	1.40	1.60
Density (ρ_m)	1.50	1.40	1.50	1.50	1.40	1.55	1.30	1.50
Jayne shape factor (S)	1.23	1.04	1.00	1.03	1.04	1.00	1.08	1.07
Dynamic shape factor (χ)	1.15	1.02	1.00	1.02	1.02	1.00	1.05	1.04
# of spectra	13	8	8	19	7	5	8	8

574

575 4. Summary and conclusions

576 This study is the first of its kind in the Czech Republic to evaluate NR-PM₁ based on its
 577 chemically speciated mass size distribution, density, shape, and origin at a rural background
 578 site. Seasonal effects and air mass variability on aerosol particles, in particular episodes of high
 579 mass and number concentrations, were investigated using highly time-resolved measurements
 580 conducted at the National Atmospheric Observatory Košetice (NAOK) during intensive
 581 campaigns in summer 2019 and winter 2020.

582 The average NR-PM₁+eBC concentrations were 8.58±3.70 µg m⁻³ in summer and 10.08±8.04
 583 µg m⁻³ in winter, with organics dominating during both seasons, followed by SO₄²⁻ in summer
 584 and NO₃⁻ in winter. The accumulation mode dominated the average mass size distributions in
 585 both seasons, with the larger particles of all species in winter as a result of aerosol ageing.
 586 Therefore, larger particles in accumulation mode are also often connected with long range
 587 transport. Organics showed the smallest modal diameter from all NR-PM₁ chemical species,
 588 which suggests its condensation on pre-existing particles.

589 The performed cluster analysis revealed rare occurrences of summer continental air masses
 590 from the SE (7%) associated with the highest concentrations of PM₁, eBC and all NR-PM₁
 591 species. Meanwhile, predominant slow winter continental air masses from the SW (44%) were
 592 associated with inversion conditions over Central Europe associated with the highest
 593 concentrations of PM₁, eBC and all NR-PM₁ species.

594 Analysis of the diurnal trend of average ρ_m showed a diurnal trend for winter that was opposite
 595 to the diurnal trend of organics, reflecting the change in aerosol composition toward local
 596 chemical formation of NO₃⁻ during the night, and probably also the change in total aerosol
 597 organics density during the day and night. The studied relationships between ρ_m (with different
 598 input of Org density), ρ_{eff} , and mass fractions of the main NR-PM₁ species suggest that the
 599 application of the density usually used in urban environments for organics (1.2 g cm⁻³) is
 600 inappropriate for rural aerosol particles due to the aging of organic aerosols and should be
 601 probably used higher value around 1.3 – 1.4 g cm⁻³.

602 Considering the seasonal differences in the χ of the episodes with high mass concentrations, the
603 χ was almost constant in summer, indicating almost spherical mainly organic particles,
604 compared to winter, indicating almost spherical shape and/or compact agglomerates with a
605 slight statistically significant decrease in χ with particle size. This could be caused by larger
606 influence of irregular BC/EC core in winter, continuously coated by both organic and inorganic
607 compounds making the larger particles more and more spherical. On the other hand, χ was
608 almost constant in the episode of high number concentrations and the shape of the particles was
609 spherical with no decreasing trend in χ with particle size.

610 By examining individual episodes of high mass and number concentrations, we show that the
611 seasonal differences in the physicochemical properties of aerosol particles were caused by the
612 diversity of sources and were related to the different air masses and meteorological conditions
613 during summer and winter season. We also confirmed the relation between particle size and age
614 reflected both in its oxidation state and shape factor. The results of these specific properties
615 (density, shape and oxidation state of particles) have general validity and thus transcend the
616 regional character of this study.

617

618 *Data availability.*

619 All relevant data for this paper is archived at the ICPF of the CAS (Institute of Chemical Process
620 Fundamentals of the Czech Academy of Sciences) and are available upon request from the
621 corresponding author (Petra Pokorná).

622 *Author contribution.*

623 PP, JS and VŽ conceived the research. PP, RL, PV, SM, AHŠ and JO conducted the
624 atmospheric aerosol measurements during both intensive campaigns. PP, NZ, RL, PV, VR and
625 JS analysed and interpreted the data. PP prepared the manuscript with contributions from all
626 co-authors.

627 *Competing interests*

628 The authors declare that they have no conflict of interest.

629 *Acknowledgements*

630 We would like to thank Daniel Vondrák for the graphical editing. Thanks also goes to American
631 Journal Experts and Laurence Windell for the English proof reading of the manuscript. The
632 authors gratefully acknowledge the NOAA Air Resources Laboratory (ARL) for the provision
633 of the HYSPLIT transport and dispersion model and/or READY website
634 (<http://www.ready.noaa.gov>) used in this publication. We greatly thank the two anonymous
635 reviewers for their effort to critically review the manuscript and for providing constructive
636 comments.

637 *Financial support*

638 This work was supported by the GACR under grant P209/19/06110Y and by the MEYS of the
639 Czech Republic under grant ACTRIS-CZ LM2018122 and ACTRIS-CZ RI
640 (CZ.02.1.01/0.0/0.0/16_013/0001315) as well as by COST Action CA16109 COLOSSAL
641 within STSM.

642 **References**

- 643 Allan, J.D., Delia, A.E., Coe, H., Bower, K.N., Alfarra, M.R., Jimenez, J.L., Middlebrook,
644 A.M., Drewnick, F., Onasch, T.B., Canagaratna, M.R., Jayne, J.T., Worsnop, D.R., 2004. A
645 generalised method for the extraction of chemically resolved mass spectra from Aerodyne
646 aerosol mass spectrometer data. *J. Aerosol Sci.* 35, 909–922.
- 647 Allan, J.D., Alfarra, M.R., Bower, K.N., Coe, H., Jayene, J.T., Worsnop, D.R., Aalto, P.P.,
648 Kulmala, M., Hyötyläinen, T., Cavalli, F., Laaksonen, A., 2006. Size and composition
649 measurements of background aerosol and new particle growth in a Finnish forest during
650 QUEST 2 using an Aerodyne Aerosol Mass Spectrometer. *Atmos. Chem. Phys.* 6, 315–327.
- 651 Belis, C.A., Karagulian, F., Larsen, B.R., Hopke, P.K., 2013. Critical review and metaanalysis
652 of ambient particulate matter source apportionment using receptor models in Europe. *Atmos.*
653 *Environ.* 69, 94–108.
- 654 Bressi, M., Cavalli, F., Putaud, J.P., Fröhlich, R., Petit, J.-E., Aas, W., Äijälä, A., Alastuey, A.,
655 Allan, J.D., Aurela, M., Berico, M., Bougiatioti, A., others. 2021. A European aerosol
656 phenomenology - 7: High-time resolution chemical characteristics of submicron particulate
657 matter across Europe. *Atmospheric Environment: X* 10, 100108, 1–16.
- 658 Carslaw, D.C., Ropkins, K., 2012. Openair – an R package for air quality data analysis. *Environ.*
659 *Model. Software* 27–28, 52–61.
- 660 Cavalli, F., Viana, M., Ytri, K.E., Genberg, J., Putaud, J.-P., 2010. Toward a standardised
661 thermal-optical protocol for measuring atmospheric organic and elemental carbon: the
662 EUSAAR protocol. *Atmospheric Measurement Techniques* 3, 79–89.
- 663 Cavallia, F., Alastue, A., Areskou, H., Ceburnis, D., Čech, J., Genber, J., Harrison, R.M.,
664 Jaffrezo, J.L., Kiss, G., Laj, P., Mihalopoulos, N., Perez, N., Quincey, P., Schwarz, J.,
665 Sellegri, K., Spindler, G., Swietlicki, E., Theodosi, C., Putaud, J.P., 2016. A European
666 aerosol phenomenology – 4: Harmonized concentrations of carbonaceous aerosol at 10
667 regional background sites across Europe. *Atmospheric Environment* 144, 133–145.
- 668 Chen, G. et al., 2021 (under review). European Aerosol Phenomenology – 8: Harmonised
669 Source Apportionment of Organic Aerosol using 22 Yearlong ACSM/AMS Datasets.
- 670 Costabile, F., Birmili, W., Klose, S., Tuch, T., Wehner, B., Wiedensohler, A., Franck, U.,
671 König, K. and Sonntag, A., 2009. Spatio-Temporal Variability and Principal Components
672 of the Particle Number Size Distribution in an Urban Atmosphere. *Atmos. Chem. Phys.* 9:
673 3163–3195.
- 674 CHMI, Tabular Survey 2019, Czech Hydrometeorological Institute (CHMI) 2019(a)
675 http://portal.chmi.cz/files/portal/docs/uoco/isko/tab_roc/2019_enh/index_GB.html, last
676 access: 4.6.2021
- 677 CHMI, Annual report 2019, Czech Hydrometeorological Institute (CHMI) 2019(b)
678 [https://www.chmi.cz/files/portal/docs/uoco/isko/grafroc/19groc/gr19cz/19_rocenka_UKO](https://www.chmi.cz/files/portal/docs/uoco/isko/grafroc/19groc/gr19cz/19_rocenka_UKO_web_tisk_up1.pdf)
679 [web_tisk_up1.pdf](https://www.chmi.cz/files/portal/docs/uoco/isko/grafroc/19groc/gr19cz/19_rocenka_UKO_web_tisk_up1.pdf), last access: 4.6.2021
- 680 Cubison, M.J., Ortega, A.M., Hayes, P.L., Farmer, D.K., Day, D., Lechner, M.J., Brune, W.H.,
681 Apel, E., Diskin, G.S., Fisher, J. a., Fuelberg, H.E., Hecobian, A., Knapp, D.J., Mikoviny,
682 T., Riemer, D., Sachse, G.W., Sessions, W., Weber, R.J., Weinheimer, A.J., Wisthaler, A.,
683 Jimenez, J.L., 2011. Effects of aging on organic aerosol from open biomass burning smoke
684 in aircraft and laboratory studies. *Atmos. Chem. Phys.* 11, 12049–12064.
- 685 Crippa, M., DeCarlo, P. F., Slowik, J. G., Mohr, C., Heringa, M. F., Chirico, R., Poulain, L.,
686 Freutel, F., Sciare, J., Cozic, J., Di Marco, C. F., Elsasser, M., Nicolas, J. B., Marchand, N.,
687 Abidi, E., Wiedensohler, A., Drewnick, F., Schneider, J., Borrmann, S., Nemitz, E.,
688 Zimmermann, R., Jaffrezo, J.-L., Prévôt, A. S. H., and Baltensperger, U. 2013. Wintertime

689 aerosol chemical composition and source apportionment of the organic fraction in the
690 metropolitan area of Paris, *Atmos. Chem. Phys.*, 13, 961-981.

691 Dall'Osto, M., Harrison, R.M., Coe, H., Williams, P.I., Allan, J.D., 2009. Real time chemical
692 characterization of local and regional nitrate aerosols. *Atmos. Chem. Phys.*, 9, 3709-3720.

693 DeCarlo, P.F., Slowik, J.G., Worsnop, D.R., Davidovits, P., Jimenez, J.L., 2004. Particle
694 Morphology and Density Characterization by Combined Mobility and Aerodynamic
695 Diameter Measurements. Part 1: Theory. *Aerosol Sci. Technol.* 38, 1185–1205.

696 Drewnick, F., Jayne, J.T., Canagaratna, M., Worsnop, D.R., Demerjian, K.L., 2004.
697 Measurement of ambient aerosol composition during the PMTACS-NY 2001 Using and
698 Aerosol Mass Spectrometer. Part II: Chemically speciated mass distribution.

699 Drewnick, F., Hings, S.S., DeCarlo, P., Jayne, J.T., Gonin, M., Fuhrer, K., Weimer, S., Jimenez,
700 J.L., Demerjian, K.L., Borrmann, S., Worsnop, R., 2005. A new Time-of-Flight Aerosol
701 Mass Spectrometer (TOF-AMS) – Instrument description and first field deployment.
702 *Aerosol Science and Technology* 39, 637–658.

703 EEA, 2019. Air Quality in Europe - 2019 Report. European Environment Agency Report
704 No 10/2019. <https://www.eea.europa.eu/publications/air-quality-in-europe-2019>.

705 Favez, O., Weber, S., Petit, J-E., Alleman, L.Y., Albinet, A., Riffault, V., Chazeau, B., Amodeo,
706 T., Salameh, D., Zhang, Y., Srivastava, S. et al., 2021. Overview of the French Operational
707 Network for In Situ Observation of PM Chemical Composition and Sources in Urban
708 Environments (CARA Program). *Atmosphere* 12, 207, 1-43.

709 Freney, E. J., Sellegri, K., Canonaco, F., Boulon, J., Hervo, M., Weigel, R., Pichon, J. M.,
710 Colomb, A., Prévôt, A.S.H., and Laj, P., 2011. Seasonal variations in aerosol particle
711 composition at the puy-de-Dôme research station in France, *Atmos. Chem. Phys.*, 11,
712 13047–13059.

713 Freney, E.J., Sellegri, K., Canonaco, F., Colomb, A., Borbon, A., Michoud, V., Doussin, J.F.,
714 Crumeyrolle, S., Amarouche, N., Pichon, J.M., Bourianne, L., Gomes, L., Prévôt, A.S.H.,
715 Beekmann, M., Schwarzenböeck, A., 2014. Characterizing the impact of urban emission on
716 regional aerosol particles: airborne measurements during the MEGAPOLI experiment.
717 *Atmos. Chem. Phys.* 14, 1397–1412.

718 Freutel, F., Schneider, J., Drewnick, von der Weiden-Reinmüller, S.L., Crippa, M., Prévôt,
719 A.S.H., Baltensperger, U., Poulain, L., Wiedensohler, A., Sciare, J., Sarda-Esteve, R.,
720 Burkhardt, J.F., Eckhardt, S., Stohl, A., Gros, V., Colomb, A., Michoud, V., Doussin, J.F.,
721 Borbon, A., Haeffelin, M., Morille, Y., Beekmann, M., Borrmann, S., 2013. Aerosol particle
722 measurements at three stationary sites in the megacity of Paris during summer 2009:
723 meteorology and air mass origin dominated aerosol particle composition and size
724 distribution. *Atmos. Chem. Phys.* 13, 933–959.

725 Fröhlich, R., Cubison, M. J., Slowik, J. G., Bukowiecki, N., Canonaco, F., Croteau, P. L., Gysel,
726 M., Henne, S., Herrmann, E., Jayne, J. T., Steinbacher, M., Worsnop, D. R., Baltensperger,
727 U., and Prévôt, A. S. H., 2015. Fourteen months of on-line measurements of the non-
728 refractory submicron aerosol at the Jungfraujoch (3580 m a.s.l.) – chemical composition,
729 origins and organic aerosol sources. *Atmos. Chem. Phys.* 15, 11373–11398.

730 Hersey, S.P., Craven, J.S., Shilling, K.A., Metcalf, A.R., Sorooshian, A., Chan, M.N., Flagan,
731 R.C., Seinfeld, J.H., 2011. The Pasadena Aerosol Characterization Observatory (PACO):
732 chemical and physical analysis of the Western Los Angeles basin aerosol. *Atmos. Chem.*
733 *Phys.* 11, 7417–7443.

734 Hinds, W. C., 1999. *Aerosol Technology*. 2nd ed. John Wiley & Sons. New York.

735 Holubová Šmejkalová, A., Zíková, N., Ždímal, V., Plachá, H., Bitter, M., 2021. Atmospheric
736 aerosol growth rates at different background station types. *Environmental Science and*
737 *Pollution Research* 28, 13352–13364.

738 Hock, N., Schneider, J., Borrmann, S., Römpf, A., Moortgat, G., Franze, T., Schauer, C.,
739 Pöschl, U., Plass-Dülmer, C., Berresheim, H., 2008. Rural continental aerosol properties and
740 processes observed during the Hohenpeissenberg Aerosol Characterization Experiment
741 (HAZE2002). *Atmos. Chem. Phys.* 8, 603–623.

742 Jayne, J. T., Leard, D. C., Zhang, X., Davidovits, P., Smith, K. A., Kolb, C. E., and Worsnop,
743 D. R., 2000. Development of an Aerosol Mass Spectrometer for Size and Composition
744 Analysis of Submicron Particles, *Aerosol Sci. Technol.*, 33, 49–70, 2000.

745 Jimenez, J. L., Jayne, J. T., Shi, Q., Kolb, C. E., Worsnop, D. R., Yourshaw, I., Seinfeld, J. H.,
746 Flagan, R. C., Zhang, X., Smith, K. A., Morris, J., and Davidovits, P., (2003a). Ambient
747 aerosol sampling using the Aerodyne Aerosol Mass Spectrometer, *J. Geophys. Res.*, 108,
748 8425.

749 Jimenez, J. L., Bahreini, R., Cocker, D. R., III, Zhuang, H., Varutbangkul, v., Flagan, R. C.
750 Seinfeld, J. H., O'Dowd, C D., and Hoffman, T (2003b). New Particle Formation from
751 Photooxidation of Diiodomethane (CH₂I₂). *J. Geophys. Res.s-Atmos.* 108(D10):AAC5/1-
752 AAC5/25.

753 Jimenez, J. L., Bahreini, R., Cocker, D. R., III, Zhuang, H., Varutbangkul, v., Flagan, R. C.,
754 Seinfeld, J. H., O'Dowd, C D., and Hoffman, T (2003c). Correction to "New Particle
755 Formation from Photooxidation of Diiodomethane (CH₂I₂)," *J. Geophys. Res.- Alm*
756 *os.*108(D23):4733.

757 Jimenez, J.L., M.R. Canagaratna, N.M. Donahue, A.S.H. Prevot, Q. Zhang, J.H. Kroll, P.F.
758 DeCarlo, J.D. Allan, H. Coe, N.L. Ng, A.C. Aiken, K.D. Docherty, I.M. Ulbrich, A.P.
759 Grieshop, A.L. Robinson, J. Duplissy, J. D. Smith, K.R. Wilson, V.A. Lanz, C. Hueglin,
760 Y.L. Sun, J. Tian, A. Laaksonen, T. Raatikainen, J. Rautiainen, P. Vaattovaara, M. Ehn, M.
761 Kulmala, J.M. Tomlinson, D.R. Collins, M.J. Cubison, E.J. Dunlea, J.A. Huffman, T.B.
762 Onasch, M.R. Alfarra, P.I. Williams, K. Bower, Y. Kondo, J. Schneider, F. Drewnick, S.
763 Borrmann, S. Weimer, K. Demerjian, D. Salcedo, L. Cottrell, R. Griffin, A. Takami, T.
764 Miyoshi, S. Hatakeyama, A. Shimono, J.Y Sun, Y.M. Zhang, K. Dzepina, J.R. Kimmel, D.
765 Sueper, J.T. Jayne, S.C. Herndon, A.M. Trimborn, L.R. Williams, E.C. Wood, C.E. Kolb,
766 A.M. Middlebrook, U. Baltensperger, and D.R. Worsnop, 2009. Evolution of Organic
767 Aerosols in the Atmosphere, *Science*, 326, 1525-1529..

768 Kozáková, J., Pokorná, P., Vodička, P., Ondráčková, L., Ondráček, J., Křůmal, K., Mikuška,
769 P., Hovorka, J., Moravec, P., Schwarz, J., 2019. Influence of regional air pollution transport
770 at a European air pollution hotspot. *Environ Sci Pollut Res* 26, 1675–1692.

771 Křůmal, K., Mikuška, P., 2020. Mass concentrations and lung cancer risk assessment of PAHs
772 bound to PM₁ aerosol in six industrial, urban and rural areas in the Czech Republic, Central
773 Europe. *Atmospheric Pollution Research* 11, 401–408.

774 Kubelová, L., Vodička, P., Schwarz, J., Cusack, M., Makeš, O., Ondráček, J., Ždímal, V., 2015.
775 A study of summer and winter high time-resolved submicron aerosol composition measured
776 at a suburban site in Prague. *Atmospheric Environment* 118, 45–57.

777 Mbengue, S., Fusek, M., Schwarz, J., Vodička, P., Holubová Šmejkalová, A. Holoubek, I.,
778 2018. Four years of highly time resolved measurements of elemental and organic carbon at
779 a rural background site in Central Europe. *Atmos. Environ.*, 182, 335–346.

780 Lide, D. R.: *CRC Handbook of Chemistry and Physics*, CRC Press Inc, USA, 1991.

781 Mbengue, S., Serfozo, N., Schwarz, J., Ziková, N., Holubová Šmejkalová, A., Holoubek, I.
782 2020. Characterization of Equivalent Black Carbon at a regional background site in Central
783 Europe: Variability and source apportionment. *Environmental Pollution* 260, 113771

784 Mikuška, P., Hopke, P.K., 2018. Source apportionment of aerosol particles at a European air
785 pollution hot spot using particle number size distributions and chemical composition.
786 *Environ. Pollut.* 234, 145–154.

787 Middlebrook, A.M., Bahreini, R., Jimenez, J.L., Canagaratna, M.R., 2012. Evaluation of
788 Composition-Dependent Collection Efficiencies for the Aerodyne Aerosol Mass
789 Spectrometer using Field Data. *Aerosol Science and Technology* 46, 258–271.

790 Milic, A., Mallet, M.D., Cravigan, L.T., Alroe, J., Ristovski, Z.D., Selleck, P., Lawson, S.J.,
791 Ward, J., Desservettaz, M.J., Paton-Walsh, C., Williams, L.R., Keywood, M.D., Miljevic,
792 B., Biomass burning and biogenic aerosols in northern Australia during the SAFIRED
793 campaign. *Atmos. Chem. Phys.* 17, 3945–3961.

794 Moffet, R. C., Qin, X. Y., Rebotier, T., Furutani, H., and Prather, K. A., 2008. Chemically
795 segregated optical and microphysical properties of ambient aerosols measured in a single-
796 particle mass spectrometer, *J. Geophys. Res.-Atmos.*, 113, D12213.

797 Ng, N.L., Canagaratna, M.R., Zhang, Q., Jimenez, J.L., Tian, J., Ulbrich, I.M., Kroll, J.H.,
798 Docherty, K.S., Chhabra, P.S., Bahreini, R., Murphy, S.M., Seinfeld, J.H., Hildebrandt, L.,
799 Donahue, N.M., DeCarlo, P.F., Lanz, V.A., Prévot, A.S.H., Dinar, E., Rudich, Y., Worsnop,
800 D.R., 2010. Organic aerosol components observed in Northern Hemispheric datasets from
801 Aerosol Mass Spectrometry. *Atmos. Chem. Phys.* 10, 4625–4641.

802 Park, K., Kittelson, D. B., Zachariah, M. R., and McMurry, P. H.: Measurement of Inherent
803 Material Density of Nanoparticle Agglomerates, *J. Nanopart. Res.*, 6, 267–272, 2004.

804 Petit, J.-E., Amodeo, T., Meleux, F., Bessagnet, B., Menut, L., Grenier, D., Pellan, Y., Ockler,
805 A., Rocq, B.; Gros, V., et al., 2017. Characterising an intense PM pollution episode in March
806 2015 in France from multi-site approach and near real time data. *Atmos. Environ.* 155, 68–
807 84.

808 Petit, J.-E., Pallarès, C., Favez, O., Alleman, L.Y., Bonnaire, N., Rivière, E., 2019. Sources and
809 Geographical Origins of PM10 in Metz (France) Using Oxalate as a Marker of Secondary
810 Organic Aerosols by Positive Matrix Factorization Analysis. *Atmosphere* 10, 370.

811 Pokorná, P., Schwarz, J., Krejci, R., Swietlicki, E., Havránek, V., Ždímal, V., 2018.
812 Comparison of PM2.5 chemical composition and sources at a rural background site in
813 Central Europe between the years 1993/1994/1995 and 2009/2010: Effect of legislative
814 regulations and economic transformation on the air quality. *Environmental Pollution* 241,
815 841-851.

816 Poulain, L., Spindler, G., Birmili, W., Plass-Dülmer, C., Wiedensohler, A., Herrmann, H., 2011.
817 Seasonal and diurnal variations of particulate nitrate and organic matter at the IfT research
818 station Melpitz. *Atmos. Chem. Phys.* 11 (24), 12579–12599.

819 Poulain, L., Spindler, G., Grüner, A., Tuch, T., Stieger, B., van Pinxteren, D., Petit, J.-E., Favez,
820 O., Herrmann, H., Wiedensohler, A., 2020. Multi-year ACSM measurements at the central
821 European Research station Melpitz (Germany) – Part 1: Instrument robustness, quality
822 assurance, and impact of upper size cutoff diameter *Atmos. Meas. Tech.*, 13, 4973–4994.

823 Putaud, J.P., Raes, F., Van Dingenen, R., Brüggemann, E., Facchini, M., Decesari, S., Fuzzi, S.,
824 Gehrig, R., Hüglin, C., Laj, P., others, 2004. A European aerosol phenomenology—2:
825 chemical characteristics of particulate matter at kerbside, urban, rural and background sites
826 in Europe. *Atmos. Environ.* 38, 2579–2595.

827 Putaud, J.P., Van Dingenen, R., Alastuey, A., Bauer, H., Birmili, W., Cyrys, J., Flentje, H.,
828 Fuzzi, S., Gehrig, R., Hansson, H.C., others, 2010. A European aerosol phenomenology —
829 3: physical and chemical characteristics of particulate matter from 60 rural, urban, and
830 kerbside sites across Europe *Atmos. Environ.* 44, 1308–1320.

831 Querol, X., Alastuey, A., Puigercus, J.A., Mantilla, E., Ruiz, C.R., Lopez-Soler, A., Plana, F.,
832 Juan, R., 1998. Seasonal evolution of suspended particles around a large coal-fired power
833 station: chemical characterization. *Atmos. Environ.* 32, 719-731.

834 Rissler, J., Nordin, E.Z., Eriksson, A.C., Nilsson, P.T., Frosch, M., Sporre, M.K., Wierzbicka,
835 A., Svenningsson, B., Löndahl, J., Messing, M.E., Sjogren, S., Hemmingsen, J.G., Loft, S.,
836 Pagels, J.H., Swietlicki, E., 2014. *Environ. Sci. Technol.* 48, 11, 6300–6308

837 Rolph, G., Stein, A., Stunder, B., 2017. Real-time environmental applications and display
838 sYstem: READY. *Environ. Model. Software* 95, 210–228.

839 Salcedo, D., Onasch, T. B., Dzepina, K., Canagaratna, M. R., Zhang, Q., Huffman, J. A.,
840 DeCarlo, P. F., Jayne, J. T., Mortimer, P., Worsnop, D. R., Kolb, C. E., Johnson, K. S.,
841 Zuberi, B., Marr, L. C., Volkamer, R., Molina, L. T., Molina, M. J., Cardenas, B., Bernabé,
842 R. M., Márquez, C., Gaffney, J. S., Marley, N. A., Laskin, A., Shutthanandan, V., Xie, Y.,
843 Brune, W., Leshner, R., Shirley, T., and Jimenez, J. L., 2006. Characterization of ambient
844 aerosols in Mexico City during the MCMA-2003 campaign with Aerosol Mass
845 Spectrometry: results from the CENICA Supersite. *Atmos. Chem. Phys.* 6, 925–946.

846 Salimi, F., Crilley, L.R., Stevanovic, S., Ristovski, Z., Mazaheri, M., He, C., Johnson, G.,
847 Ayoko, G., Morawska, L., 2015. Insights into the growth of newly formed particles in a
848 subtropical urban environment. *Atmos. Chem. Phys.* 15, 13475–13485.

849 Schwarz, J., Chi, X., Maenhaut, W., Civis, M., Hovorka, J., Smolík, J., 2008. Elemental and
850 organic carbon in atmospheric aerosols at downtown and suburban sites in Prague. *Atmos.*
851 *Res.* 90, 287-302.

852 Schwarz, J., Štefancová, L., Maenhaut, W., Smolík, J., Ždímal, V., 2012. Mass and chemically
853 speciated size distribution of Prague aerosol using an aerosol dryer – The influence of air
854 mass origin. *Science of the Total Environment*

855 Schwarz, J., Cusack, M., Karban, J., Chalupníčková, E., Havránek, V., Smolík, J., Ždímal, V.,
856 2016. PM_{2.5} chemical composition at a rural background site in Central Europe, including
857 correlation and air mass back trajectory analysis. *Atmospheric Research* 176–177, 108–20.

858 Seinfeld, J.H., Pandis, S.N., 2006. *Atmospheric Chemistry and Physics*. John Wiley & Sons,
859 New York.

860 Slowik, J.G., Stainken, K., Davidovits, P., Williams, L.R., Jayne, J.T., Kolb, C.E., Worsnop,
861 D.R., Rudich, Y., DeCarlo, P.F., Jimenez, J.L., 2004. Particle Morphology and Density
862 Characterization by Combined Mobility and Aerodynamic Diameter Measurements. Part 2:
863 Application to Combustion-Generated Soot Aerosols as a Function of Fuel Equivalence
864 Ratio *Aerosol Science and Technology*, 38, 1206-1222.

865 Takegawa, N., Miyazaki, Y., Kondo, Y., Komazaki, Y., Miyakawa, T., Jimenez, J.L., Jayne,
866 J.T., Worsnop, D.R., Allan, J.D., Weber, R.J., 2005. Characterization of an Aerodyne
867 Aerosol Mass Spectrometer (AMS): Intercomparison with Other Aerosol Instruments,
868 *Aerosol Science and Technology*, 39:8, 760-770.

869 Turpin, B. J. and Lim, H.-J., 2001. Species contributions to PM_{2.5} mass concentrations:
870 revisiting common assumptions for estimating organic mass, *Aerosol Sci. Tech.*, 35, 302–
871 610.

872 Vodička, P., Kawamura, K., Schwarz, J., Kunwar, B., Zdímal, V., 2019. Seasonal study of
873 stable carbon and nitrogen isotopic composition in fine aerosols at a Central European rural
874 background station. *Atmos. Chem. Phys.* 19, 3463–3479.

875 Vu, T.V., Delgado-Saborit, J.M., Harrison, R.M., 2015. Review: particle number size
876 distributions from seven major sources and implications for source apportionment studies.
877 *Atmos. Environ.* 122, 114–132.

878 Waked, A., Favez, O., Alleman, L.Y., Piot, C., Petit, J.-E., Delaunay, T., Verlinden, E., Golly,
879 B., Besombes, J.-L., Jaffrezo, J.-L., 2014. Source apportionment of PM₁₀ in a north-western
880 Europe regional urban background site (Lens, France) using positive matrix factorization
881 and including primary biogenic emissions. *Atmos. Chem. Phys.* 14, 3325–3346.

882 Wickham, H., 2016. *ggplot2: Elegant Graphics for Data Analysis*. Springer-Verlag, New York.

883 Wiedensohler, A., Wiesner, A., Weinhold, K., Birmili, W., Hermann, H., Merkel, M., Müller,
884 T., Pfeifer, S., Schmidt, A., Tuch, T., Velarde, F., Quincey, P., Seeger, S., Nowak, A., 2017.

885 Mobility particle size spectrometers: Calibration procedures and measurement uncertainties.
886 *Aerosol Science and Technology*, 52:2, 146-164.

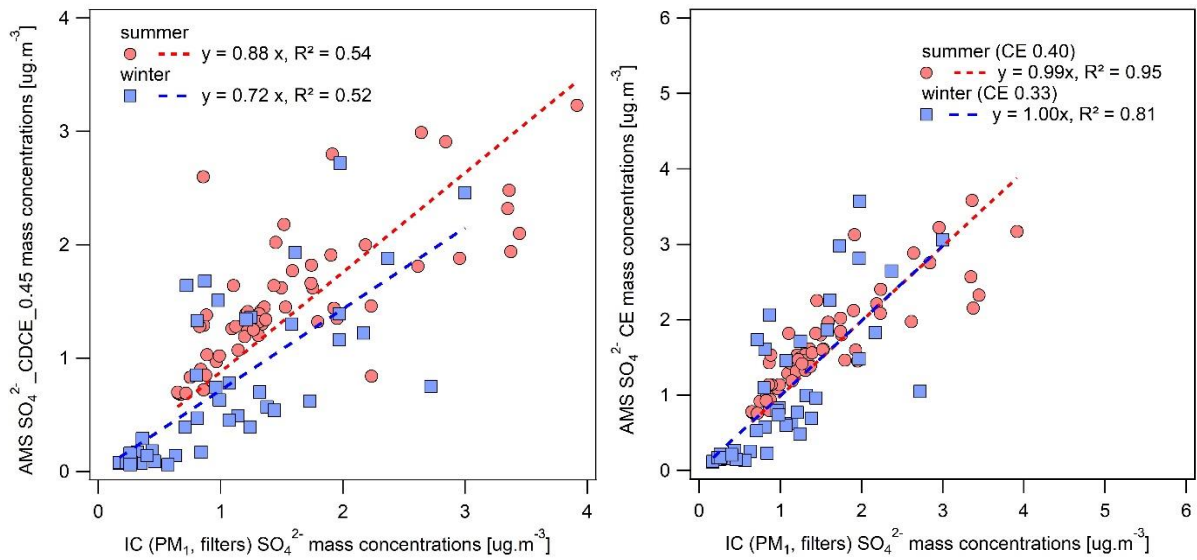
887 Zelenyuk, A., Cai, Y., Imre, D., 2006. From Agglomerates of Spheres to Irregularly Shaped
888 Particles: Determination of Dynamic Shape Factors from Measurements of Mobility and
889 Vacuum Aerodynamic Diameters. *Aerosol Science and Technology*, 40, 197–217.

890 Zíková, N., Ždímal, V., 2013. Long-Term Measurement of Aerosol Number Size Distributions
891 at Rural Background Station Košetice. *Aerosol and Air Quality Research*, 13, 1464–1474.

892 Zíková, N., Ždímal, V., 2016. Precipitation scavenging of aerosol particles at a rural site in the
893 Czech Republic. *Tellus B: Chemical and Physical Meteorology* 68, 27343, 1–14.

894
895
896
897
898
899
900
901
902
903
904
905
906
907
908
909
910
911
912
913
914
915
916
917
918
919
920
921
922
923

924 **APPENDIX**

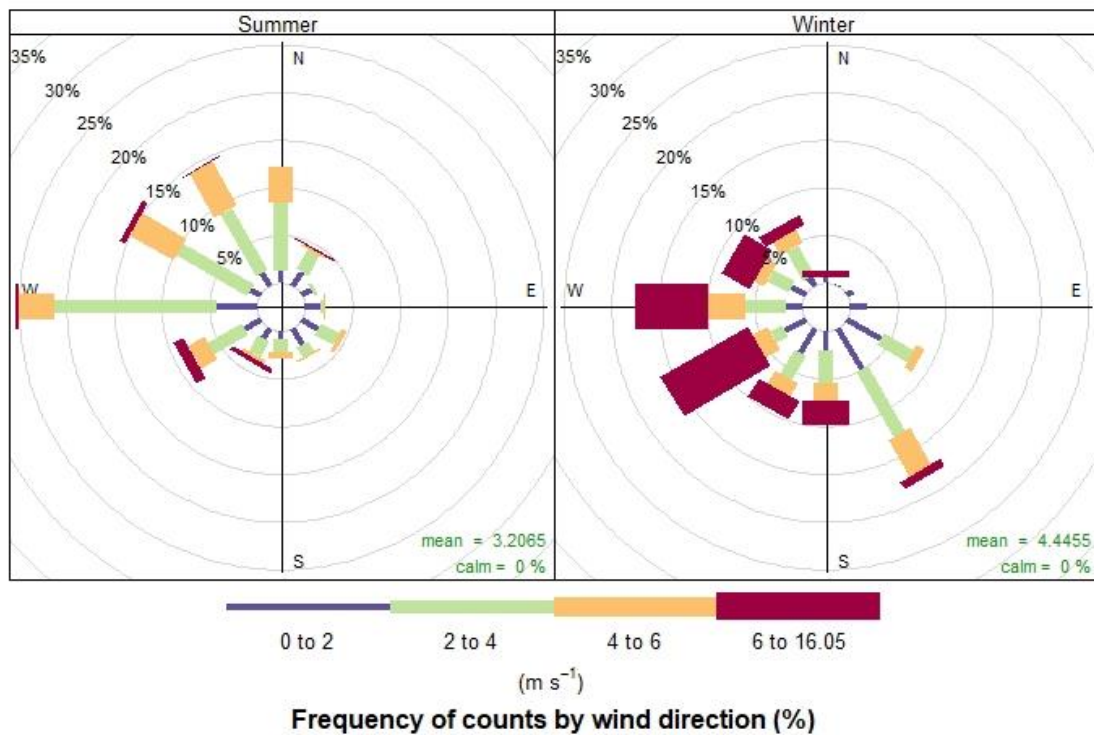


925

926 Figure A1. Comparison of sulphate concentrations measured by AMS and retrieved from PM₁
 927 filter analysis by IC with applied CDCE correction (left) and constant CE correction (right) for
 928 both measurement seasons.

929

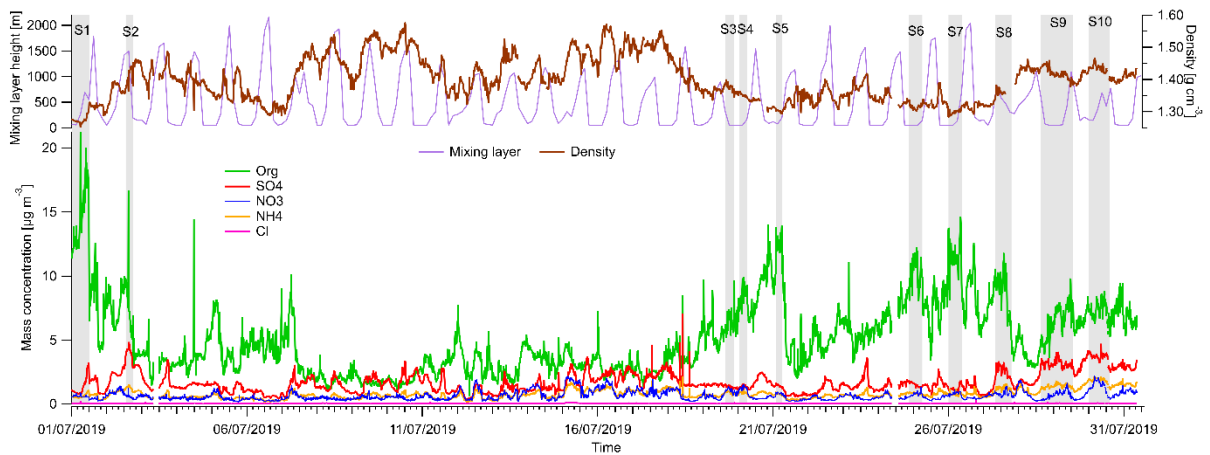
930



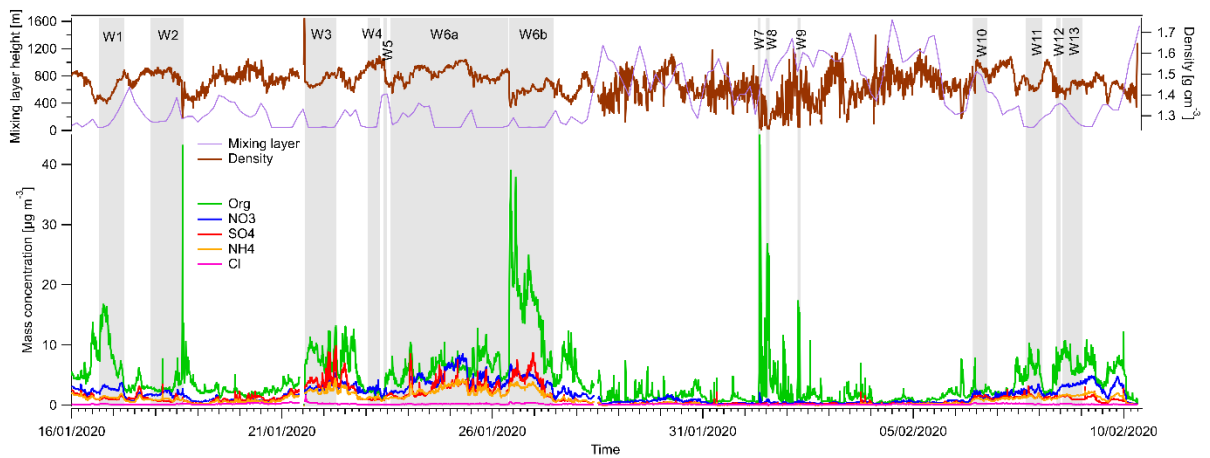
931

932 Figure A2. Wind rose summer and winter.

933



934

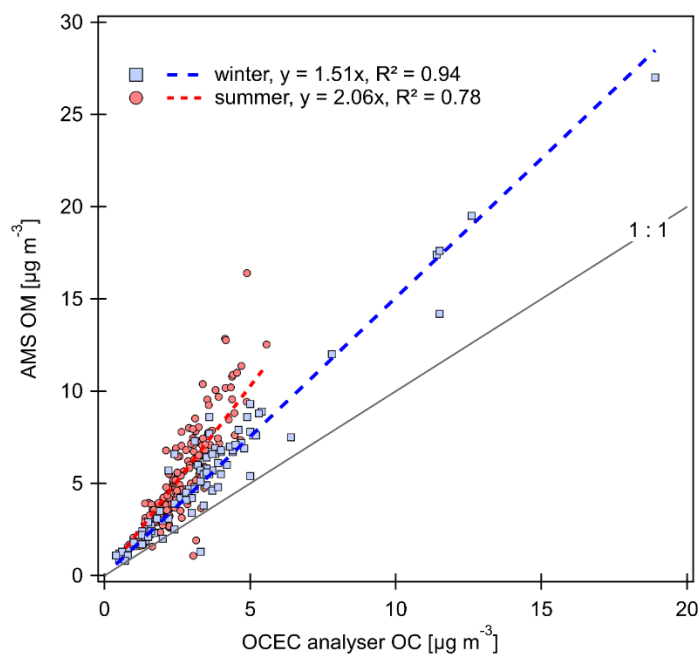


935

936 Figure A3. Mass concentration of Org, NO₃⁻, SO₄²⁻, and NH₄⁺ measured by AMS with applied
937 constant collection efficiency (CE) correction for summer (top) and winter (bottom) campaign
938 with marked episodes of higher mass concentrations, mixing layer height and particle effective
939 density calculated using Eq. (2) in the main text from Salcedo et al., 2006.

940

941



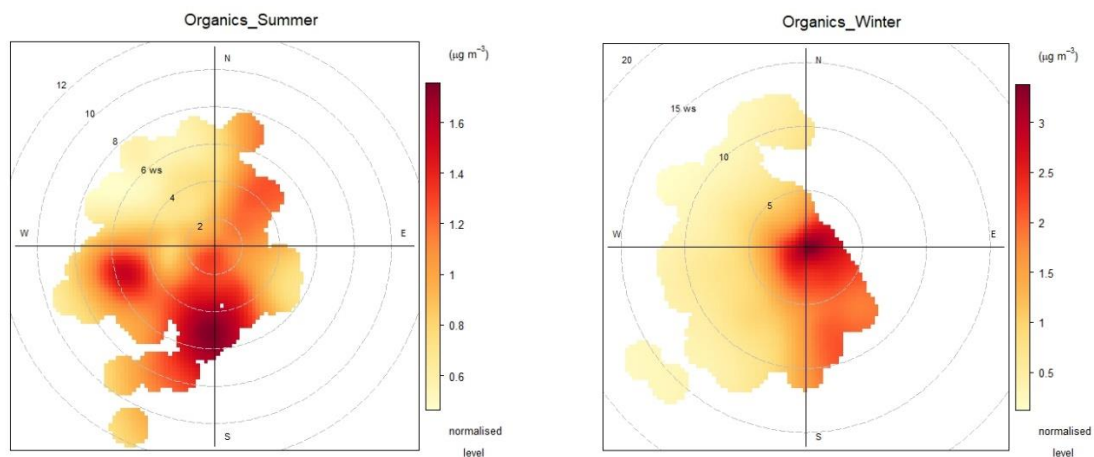
942

943 Figure A4. Comparison of organic mass concentration measured on-line by AMS (Org CE
 944 corrected) and by OCEC analyser in summer and winter.

945

946

947



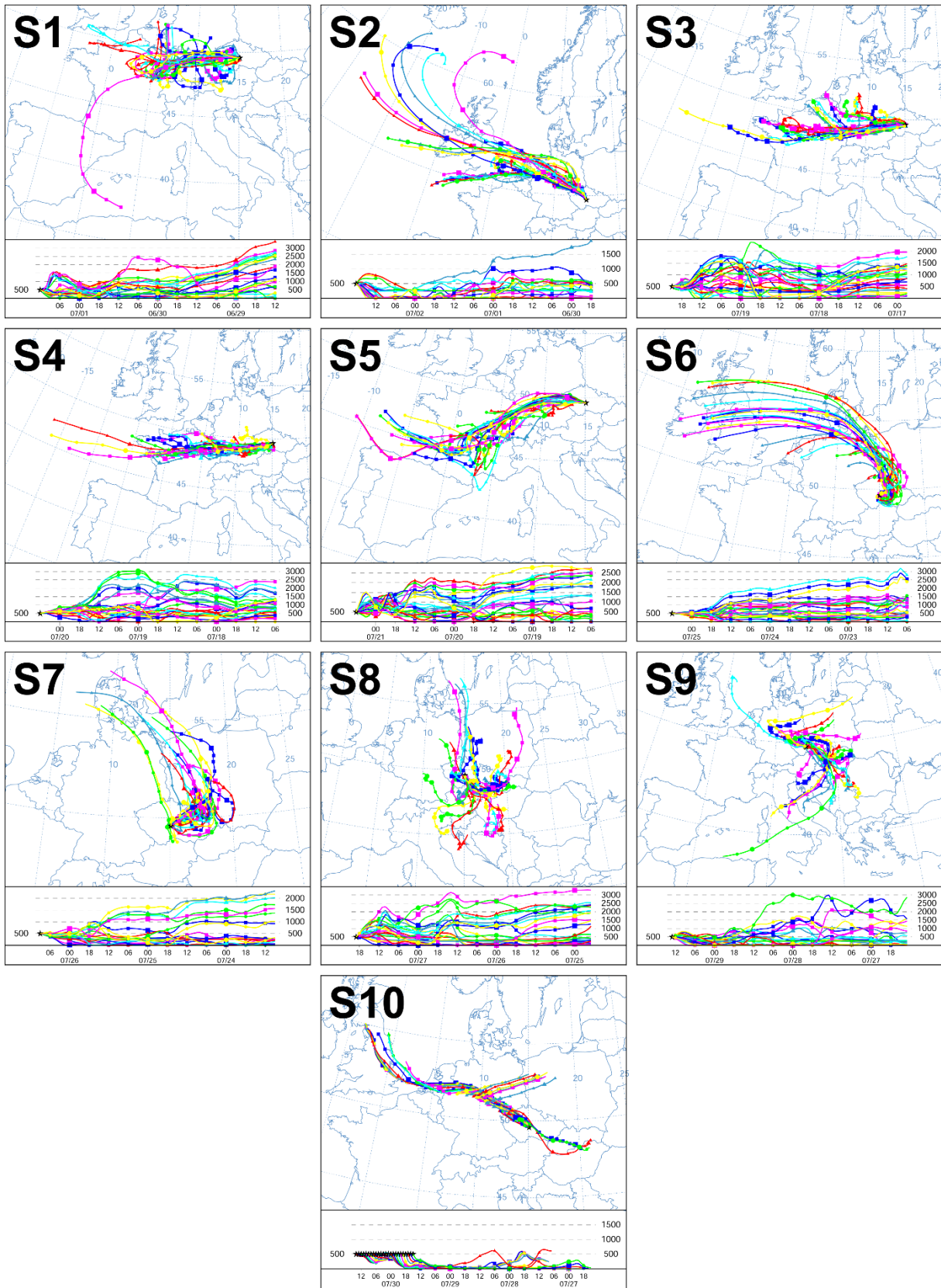
948

949 Figure A5. Polar plots showing the origin of organics in summer (left) and winter (right).

950 Table A1. Overview table presenting mass (M) and median diameter (d) of NR-PM₁ species calculated by
 951 fitting log-normal function to the AMS size distributions for the selected episodes in summer (S1 – S10) and
 952 winter (W1 – 13) along with meteorology recorded during the episodes (relative humidity – RH, global
 953 radiation – GR, temperature – T, wind speed – WS and wind direction – WD)

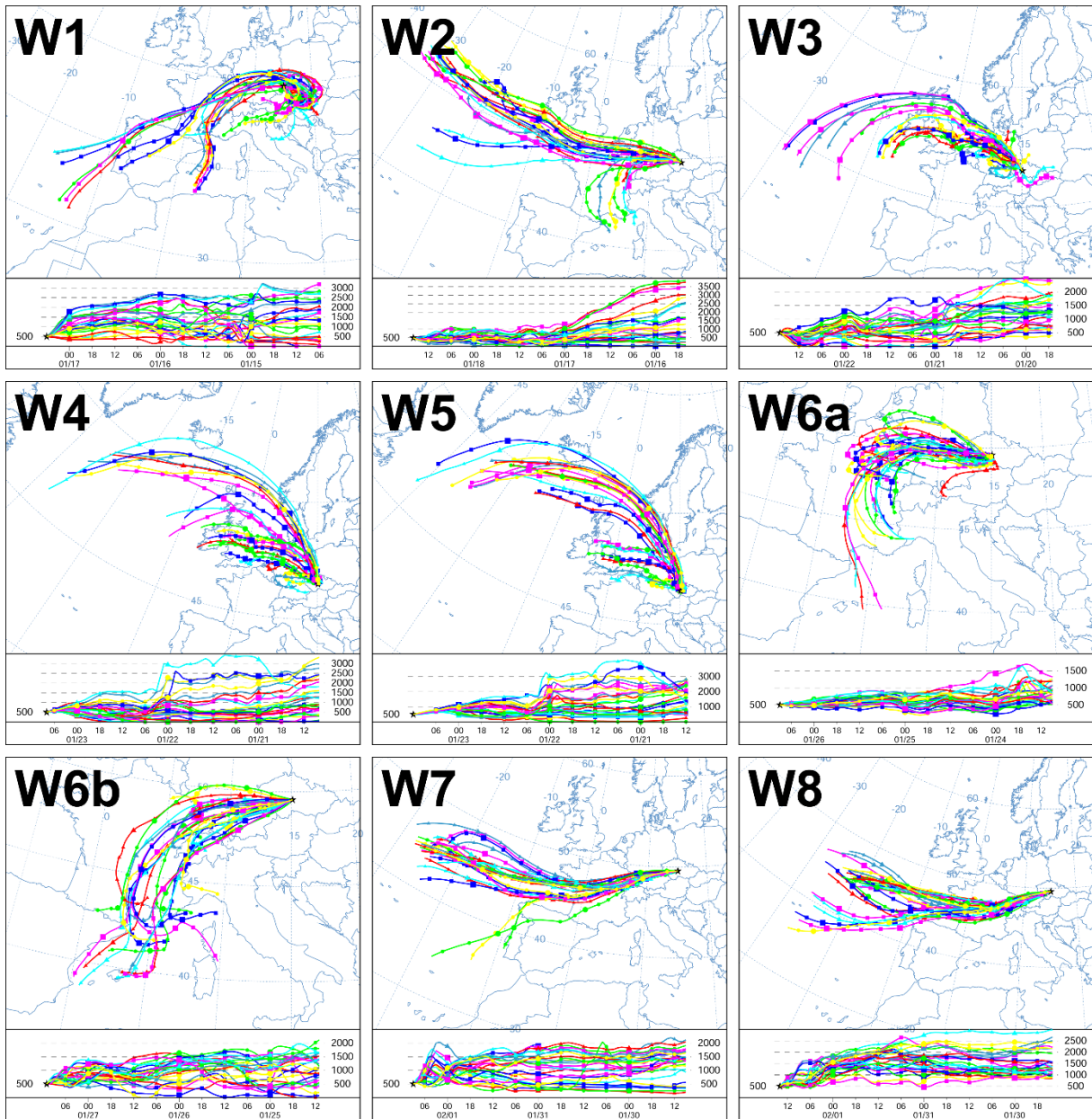
Episode	Start	End	Duration [h]	M_Org [ug m ⁻³]	M_NO ₃ ⁻ [ug m ⁻³]	M_SO ₄ ²⁻ [ug m ⁻³]	M_NH ₄ ⁻ [ug m ⁻³]	d_Org [nm]	d_NO ₃ ⁻ [nm]	d_SO ₄ ²⁻ [nm]	d_NH ₄ ⁻ [nm]
S1	7.1.19 0:00	7.1.19 12:00	12	14.58	0.82	1.24	0.91	314	285	414	498
S2	7.2.19 13:00	7.2.19 18:00	5	6.33	0.49	4.70	1.52	307	304	325	335
S3	7.19.19 15:00	7.19.19 21:00	6	6.71	2.00	1.84	1.15	373	421	470	453
S4	7.20.19 1:00	7.20.19 6:00	5	8.41	2.03	1.58	1.21	365	388	467	466
S5	7.21.19 2:00	7.21.19 6:00	4	10.83	1.01	1.53	0.95	358	333	473	504
S6	7.24.19 21:00	7.25.19 6:00	9	8.94	0.97	1.59	1.07	284	271	366	412
S7	7.26.19 0:00	7.26.19 9:00	9	9.25	0.98	1.43	0.99	279	253	382	454
S8	7.27.19 8:00	7.27.19 18:59	10	9.63	1.36	3.54	1.56	399	412	439	436
S9	7.28.19 15:00	7.29.19 13:00	22	6.78	1.16	4.49	1.76	409	414	430	439
S10	7.30.19 0:00	7.30.19 14:00	14	9.57	3.37	6.14	2.98	466	491	494	478
W1	1.16.20 15:30	1.17.20 6:00	14.5	8.60	5.63	1.39	3.47	357	378	447	392
W2	1.17.20 21:00	1.18.20 16:00	19	4.04	5.84	1.45	3.83	356	428	456	429
W3	1.21.20 13:00	1.22.20 17:00	28	9.33	7.50	7.13	7.90	563	609	636	607
W4	1.23.20 1:00	1.23.20 8:00	7	1.90	7.04	1.89	4.48	388	386	487	410
W5	1.23.20 10:00	1.23.20 12:00	2	4.26	7.27	3.20	5.46	357	386	433	391
W6	1.23.20 14:00	1.27.20 11:00	93	7.82	9.40	4.18	6.76	460	586	630	588
W6a	1.23.20 14:00	1.26.20 9:00	67	6.18	10.66	4.15	7.55	523	584	629	584
W6b	1.26.20 9:30	1.27.20 11:00	25.5	13.23	6.37	4.34	4.89	398	571	625	593
W7	2.1.20 7:30	2.1.20 9:00	1.5	15.63	0.93	0.74	0.96	336	276	241	390
W8	2.1.20 12:00	2.1.20 14:00	2	10.32	0.72	0.62	0.90	295	240	242	365
W9	2.2.20 6:00	2.2.20 7:30	1.5	10.12	0.17	0.41	0.76	296	787	287	392
W10	2.6.20 10:00	2.6.20 18:00	8	2.15	2.66	4.19	3.35	385	479	473	462
W11	2.7.20 16:00	2.8.20 1:30	9.5	5.76	5.09	2.50	3.30	366	419	488	446
W12	2.8.20 9:30	2.8.20 12:00	2.5	6.52	5.23	2.27	3.06	387	461	523	478
W13	2.8.20 13:00	2.9.20 0:30	11.5	7.72	8.12	1.93	4.35	379	436	498	451
Episode	Start	End	Duration [h]	RH [%]	GR [W m ⁻²]	T [°C]	WS [m s ⁻¹]	WD			
S1	7.1.19 0:00	7.1.19 12:00	12	49	318	25.8	3.7	W-SW			
S2	7.2.19 13:00	7.2.19 18:00	5	44	566	22.8	3.7	N-NNW			
S3	7.19.19 15:00	7.19.19 21:00	6	91	92	17.3	1.5	S-SE-W			
S4	7.20.19 1:00	7.20.19 6:00	5	97	28	14.9	1.3	SE			
S5	7.21.19 2:00	7.21.19 6:00	4	68	31	19.7	2.5	SW-NW			

S6	7.24.19 21:00	7.25.19 6:00	9	68	13	18.2	1.2	SW-SE
S7	7.26.19 0:00	7.26.19 9:00	9	59	148	19.1	2.3	W
S8	7.27.19 8:00	7.27.19 18:59	10	75	297	21.3	3.4	SE
S9	7.28.19 15:00	7.29.19 13:00	22	81	156	20.5	2.4	W-NW-SE
S10	7.30.19 0:00	7.30.19 14:00	14	81	196	20.9	3.7	W
W1	1.16.20 15:30	1.17.20 6:00	14.5	92	3	1.1	2.1	SE
W2	1.17.20 21:00	1.18.20 16:00	19	96	13	0.4	2.0	SE-NW
W3	1.21.20 13:00	1.22.20 17:00	28	93	77	-3.8	2.5	NW-SE
W4	1.23.20 1:00	1.23.20 8:00	7	88	0	0.1	1.7	W-NW
W5	1.23.20 10:00	1.23.20 12:00	2	73	120	0.6	1.9	SE
W6	1.23.20 14:00	1.27.20 11:00	93	93	34	-1.1	1.7	SE-S-SW
W6a	1.23.20 14:00	1.26.20 9:00	67	94	20	-2.4	2.0	SE-S
W6b	1.26.20 9:30	1.27.20 11:00	25.5	98	43	-1.0	1.1	SE
W7	2.1.20 7:30	2.1.20 9:00	1.5	77	22	9.2	3.9	SW
W8	2.1.20 12:00	2.1.20 14:00	2	69	201	11.9	7.5	SW
W9	2.2.20 6:00	2.2.20 7:30	1.5	75	0	4.1	8.1	W
W10	2.6.20 10:00	2.6.20 18:00	8	76	112	0.4	6.0	W-NW
W11	2.7.20 16:00	2.8.20 1:30	9.5	92	4	0.9	1.5	SE
W12	2.8.20 9:30	2.8.20 12:00	2.5	85	237	0.8	3.9	SE
W13	2.8.20 13:00	2.9.20 0:30	11.5	84	86	0.6	2.7	SW-SE



956

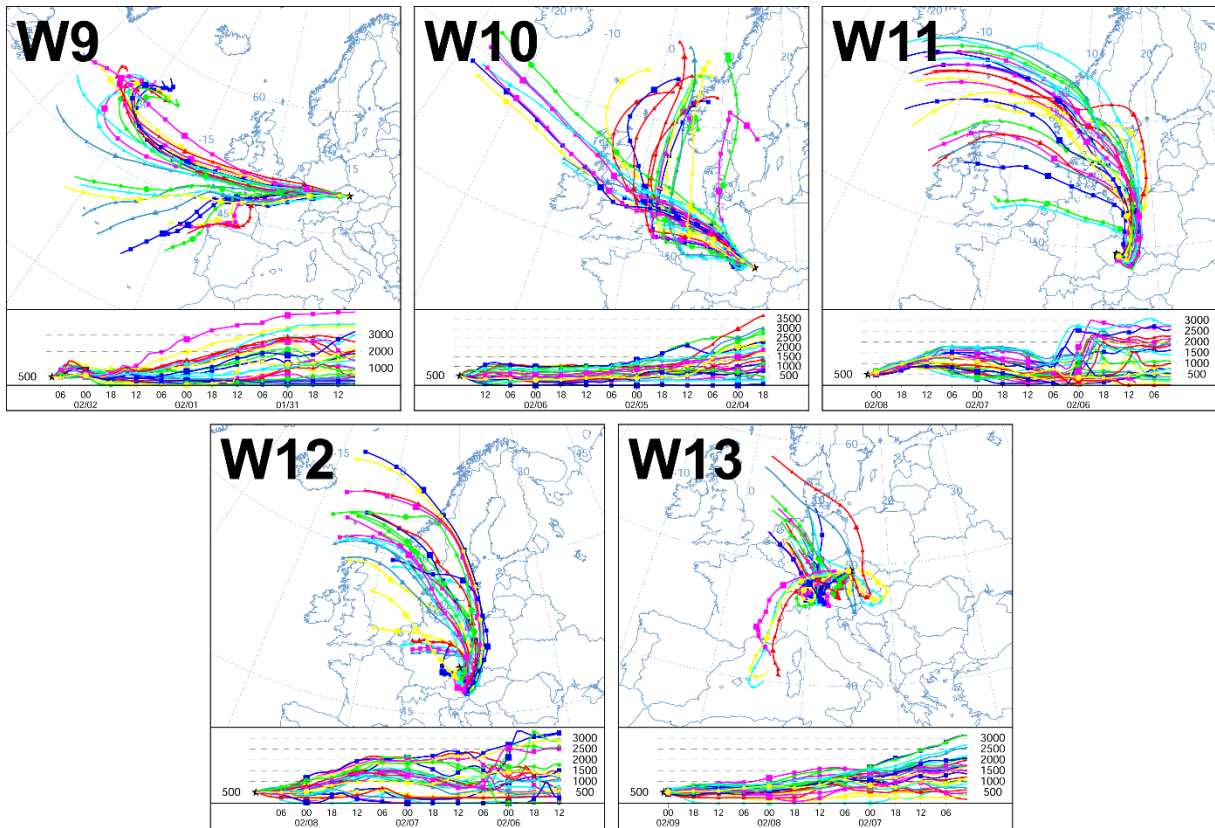
957 Figure A5. Backward air mass trajectories calculated by HYSPLIT for corresponding summer
 958 episodes (S1 – S10) of high concentration of species size distributions.



960

961 Figure continues.

962



963

964

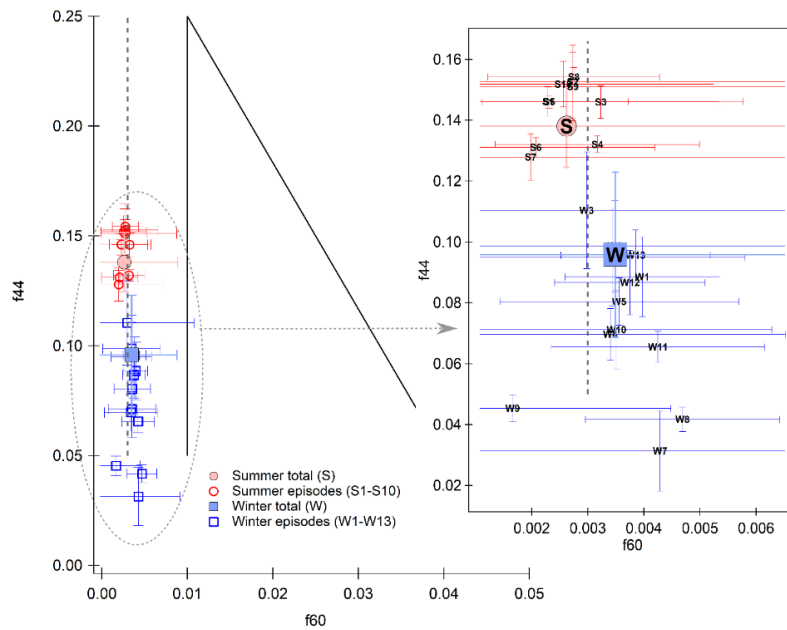
965 Figure A6. Backward air mass trajectories calculated by HYSPLIT for corresponding winter
 966 episodes (W1 – W13) of high concentration of species size distributions.

967

968

969

970

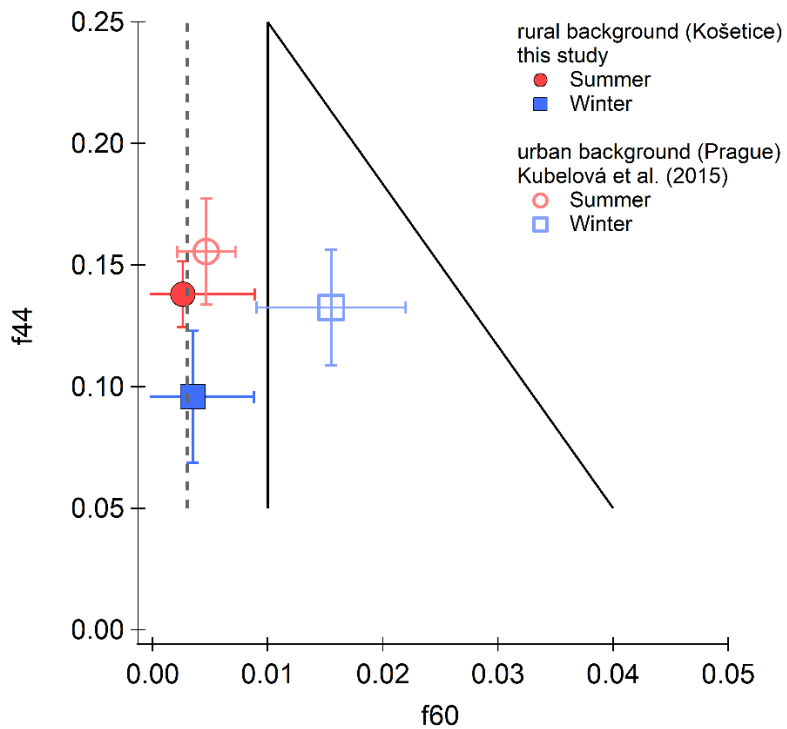


971

972 Figure A7. Comparison of organic fragments f_{44} and f_{60} for the whole campaigns (full markers)
 973 and for the specific episodes (empty markers). Bars represent standard deviation and the
 974 triangular space area of biomass burning (BB) influence and dashed line a limit for a negligible
 975 fresh BB influence (Cubison et al., 2011).

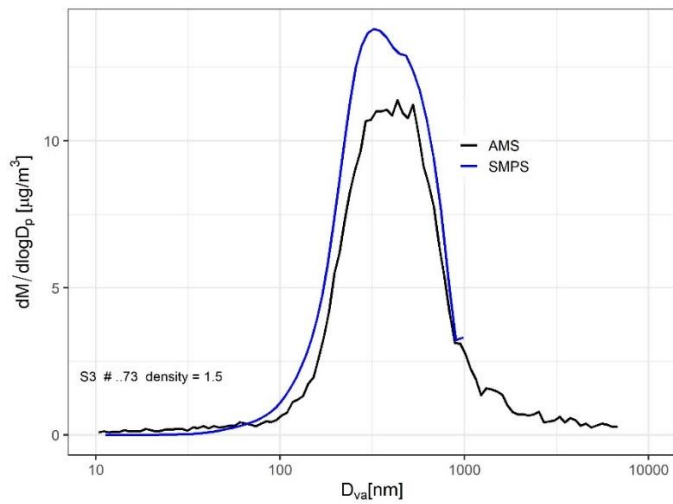
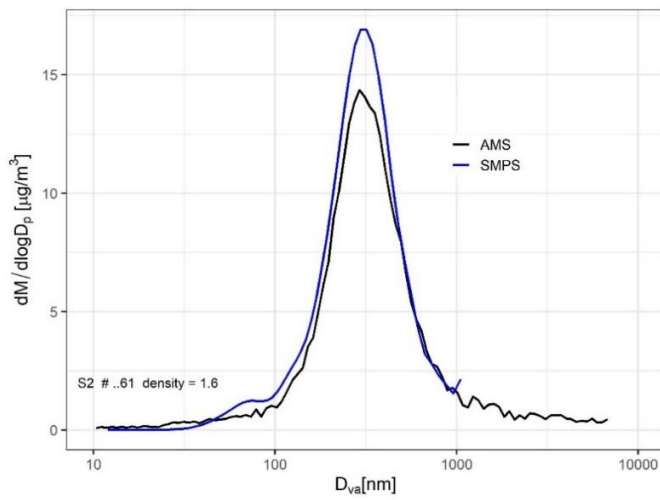
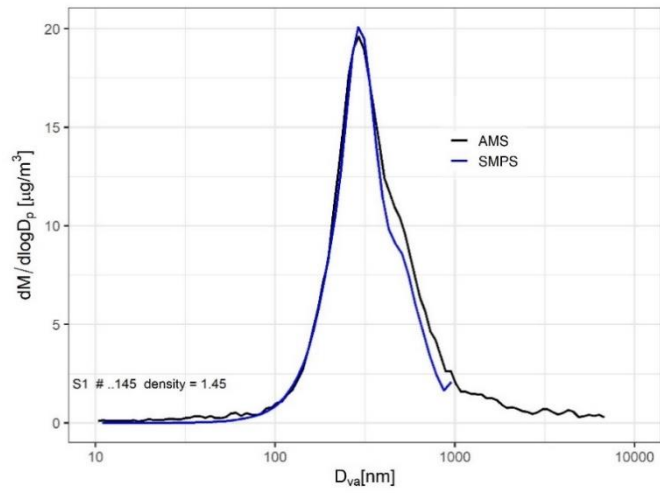
976

977



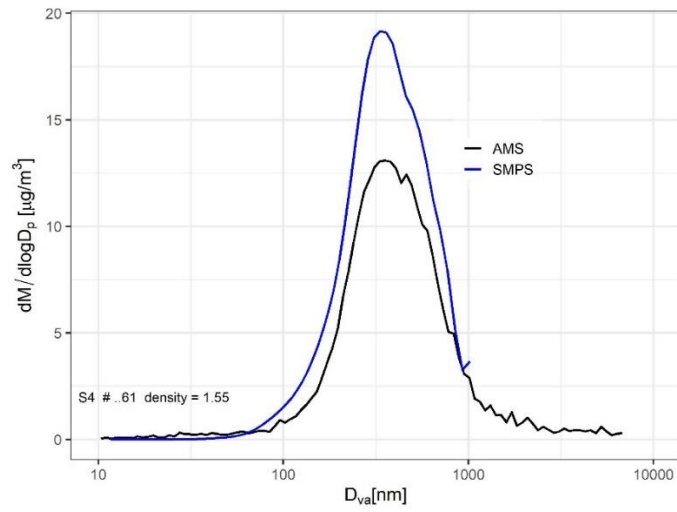
978

979 Figure A8. Comparison of organic fragments f_{44} and f_{60} determined at rural background site
 980 (NAOK) and urban background site (Prague, study by Kubelová et al., 2015) during summer
 981 and winter seasons

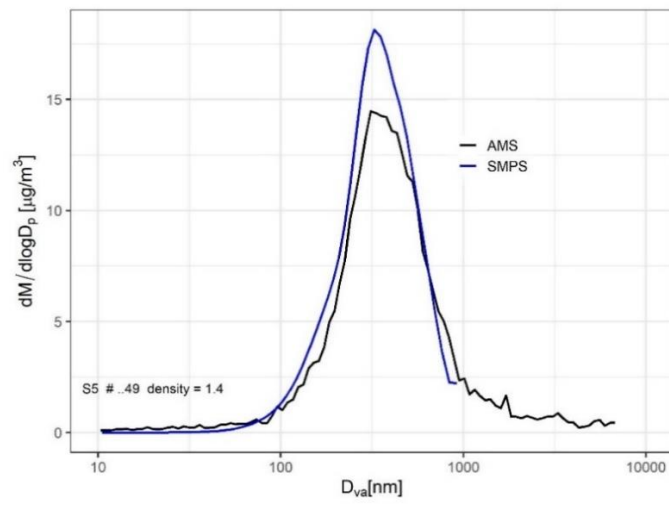


982

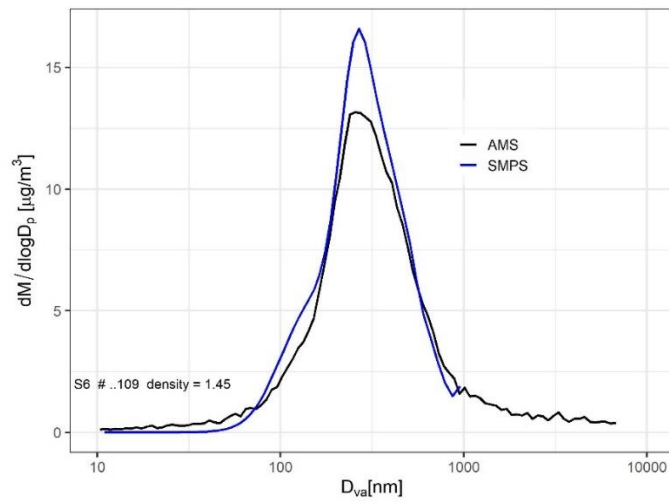
983



984

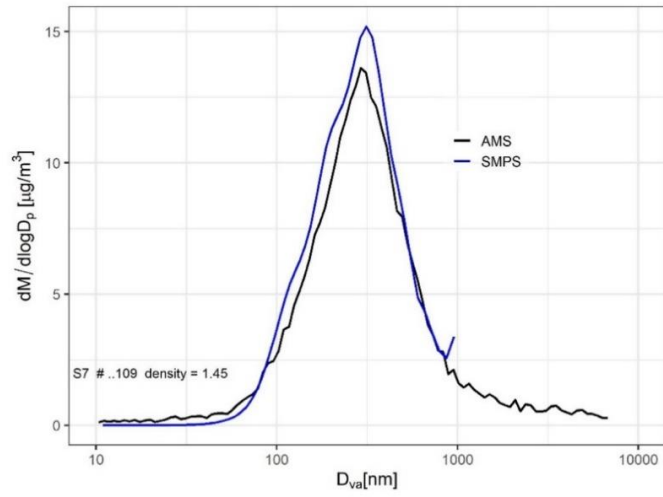


985

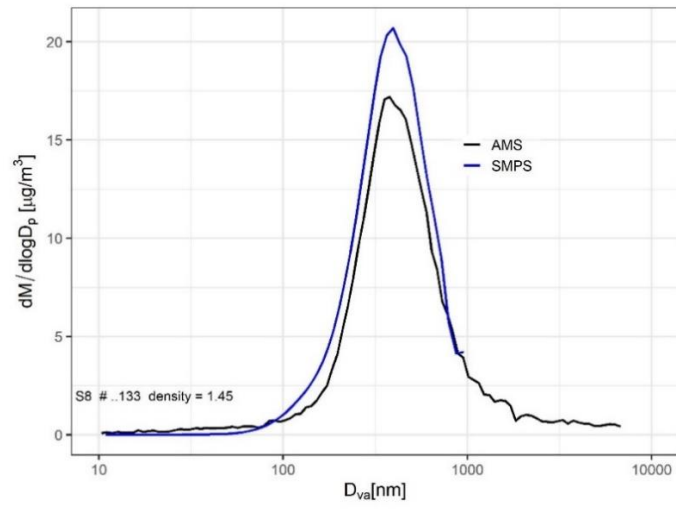


986

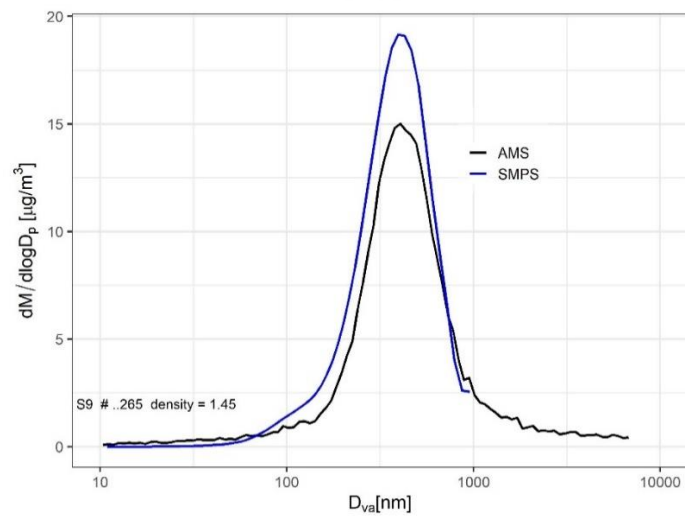
987

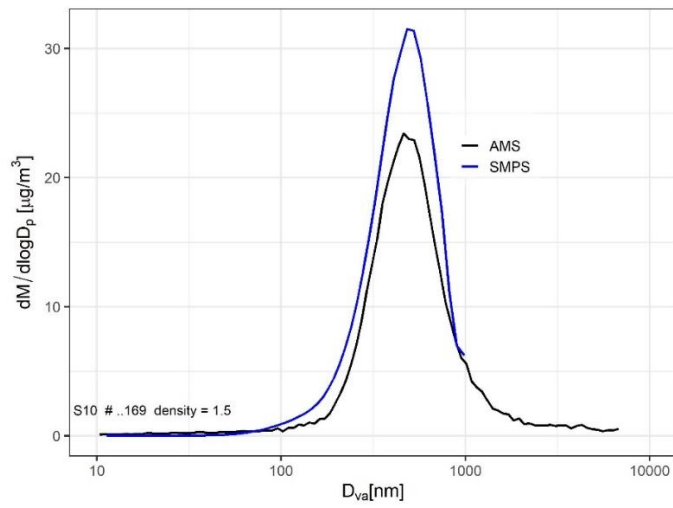


988



989



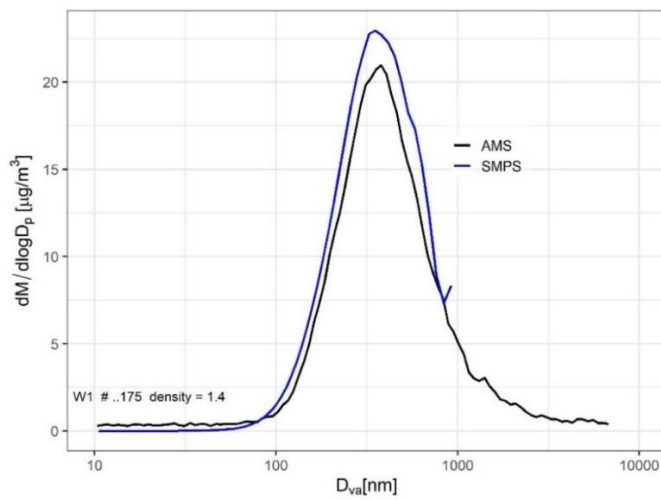


990

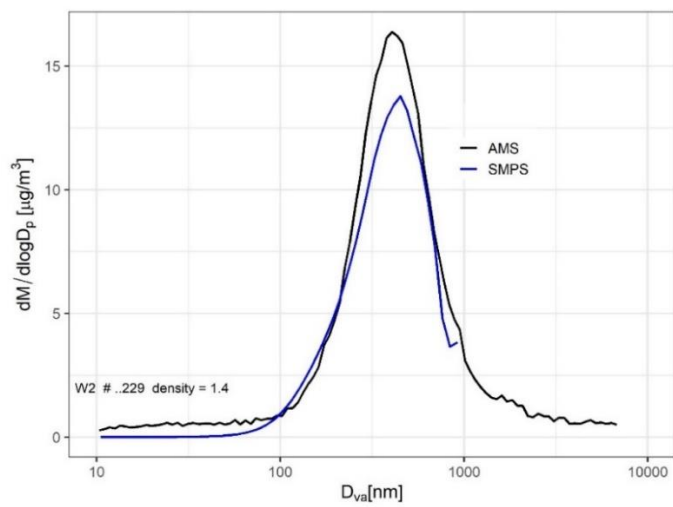
991 Figure A9. Fit of AMS and MPSS mass size distribution spectra of summer episodes (S1 –
 992 S10) for density calculation.

993

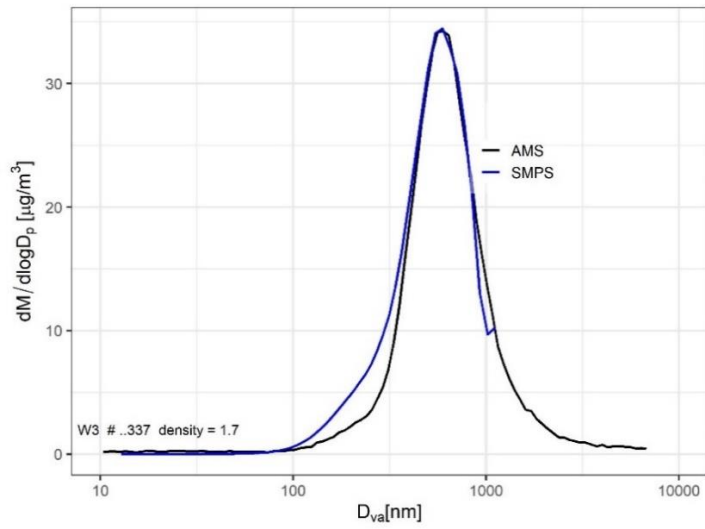
994



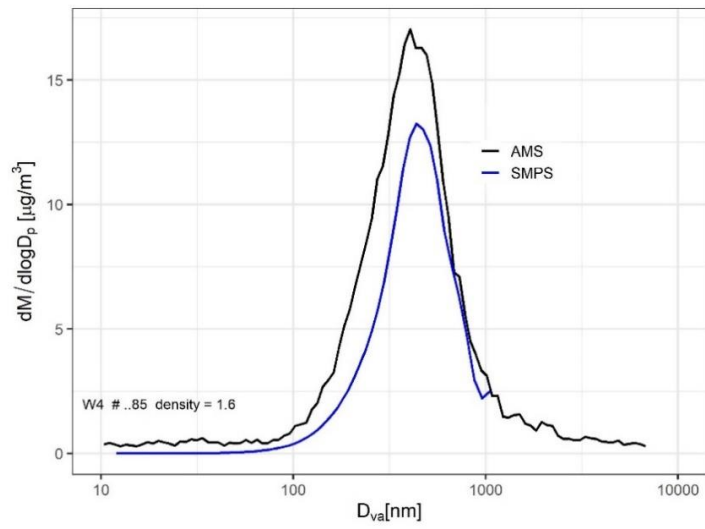
995



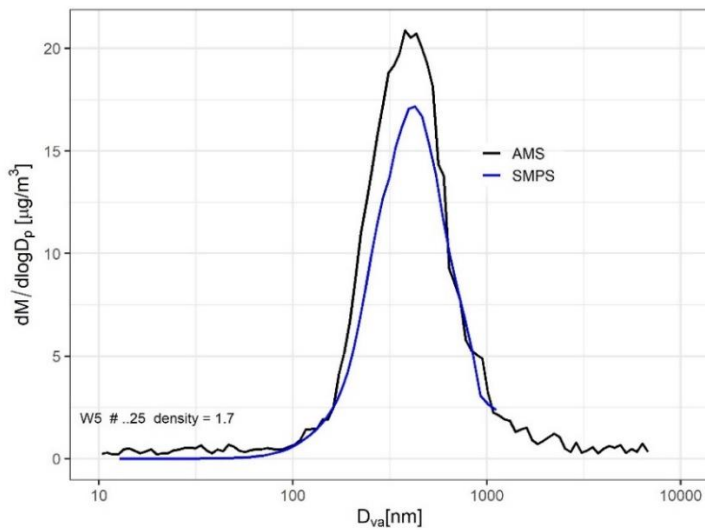
996



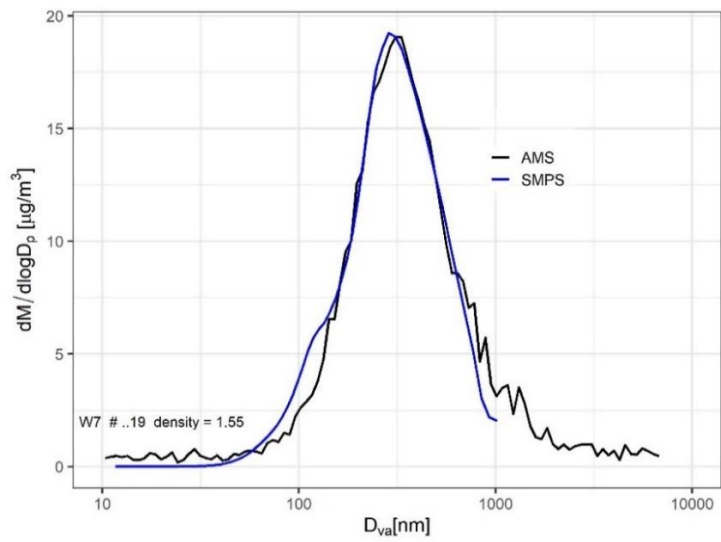
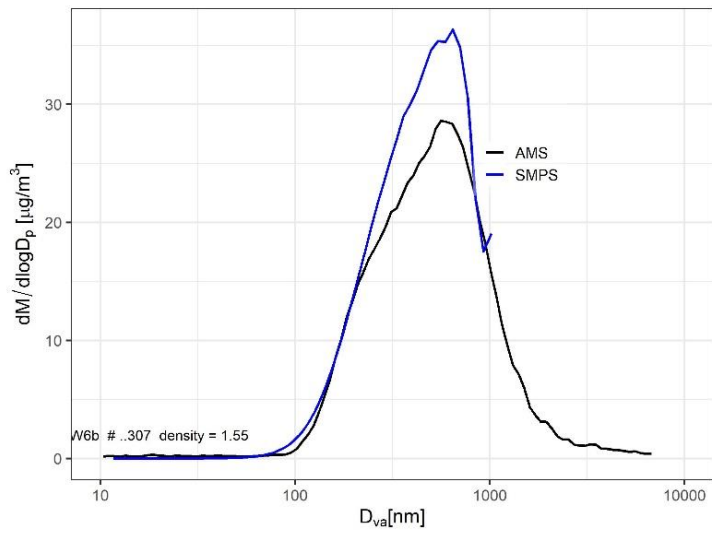
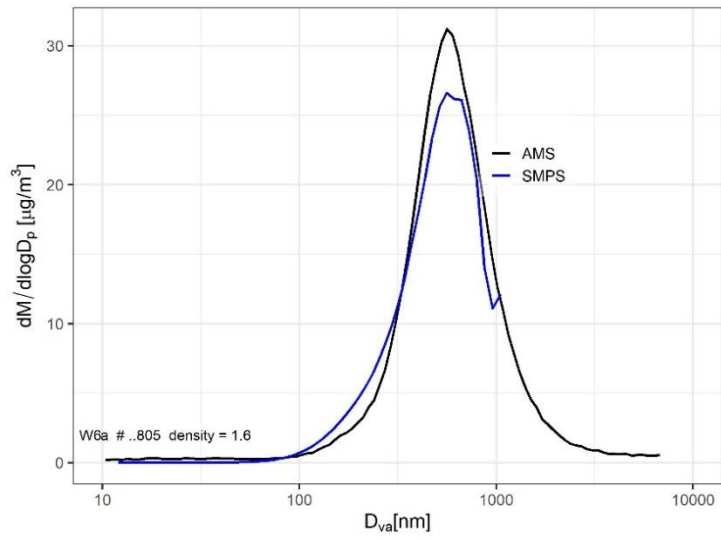
997

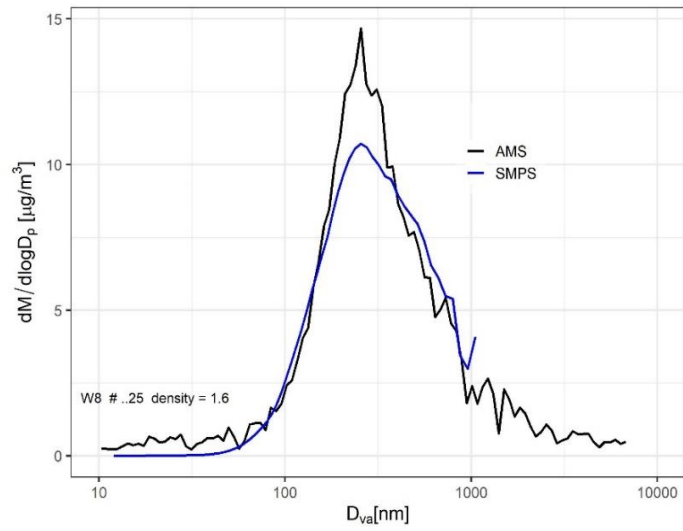


998
999

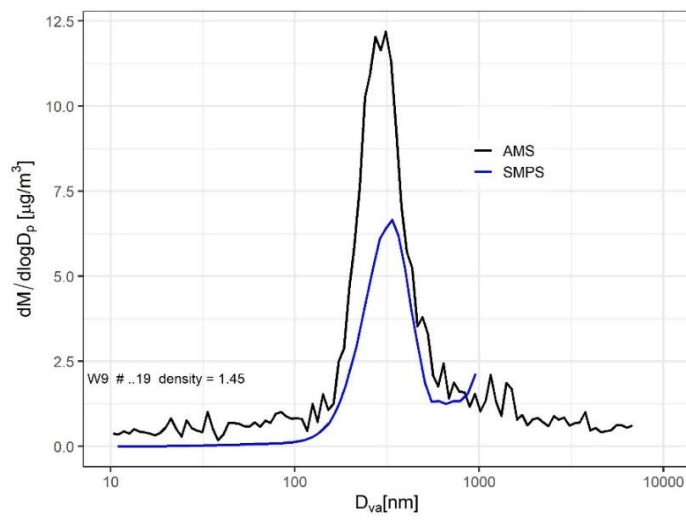


1000

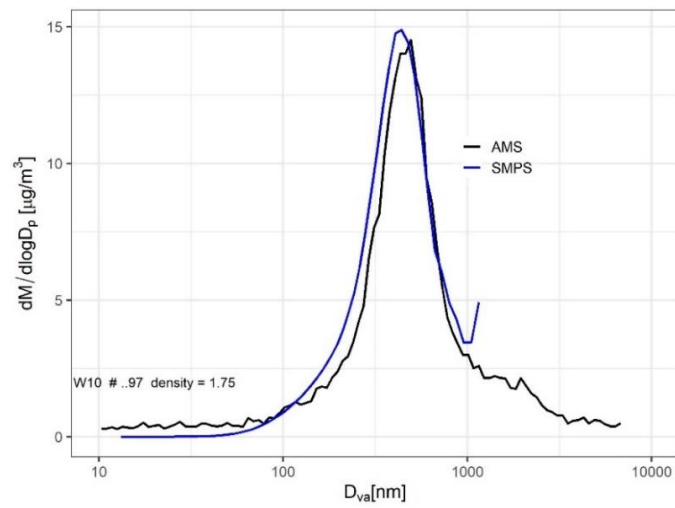




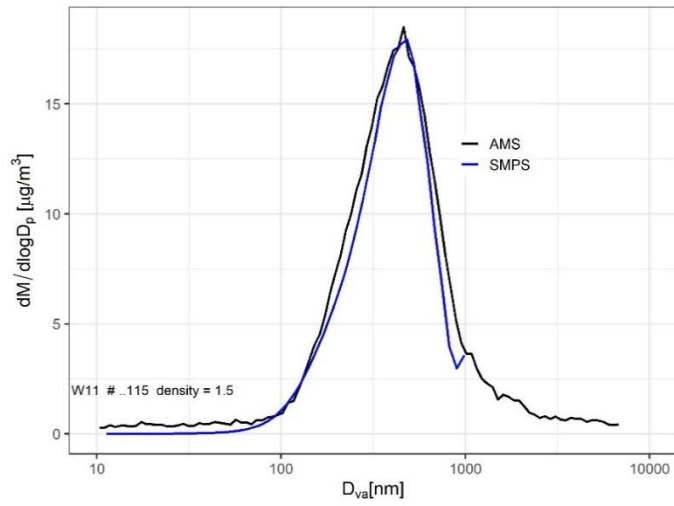
1004



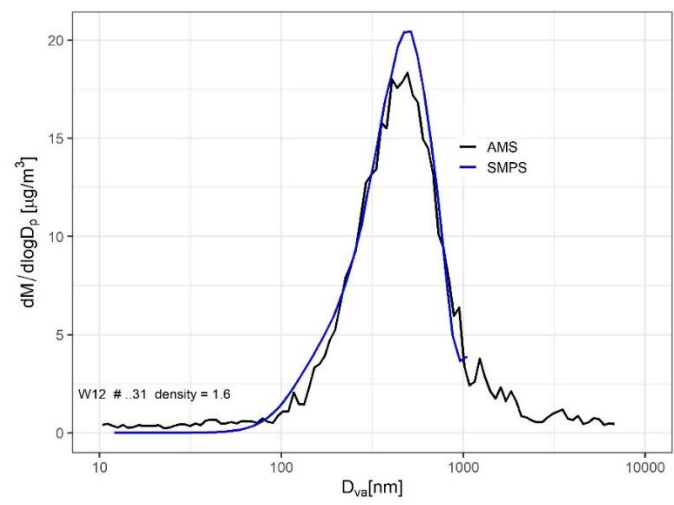
1005



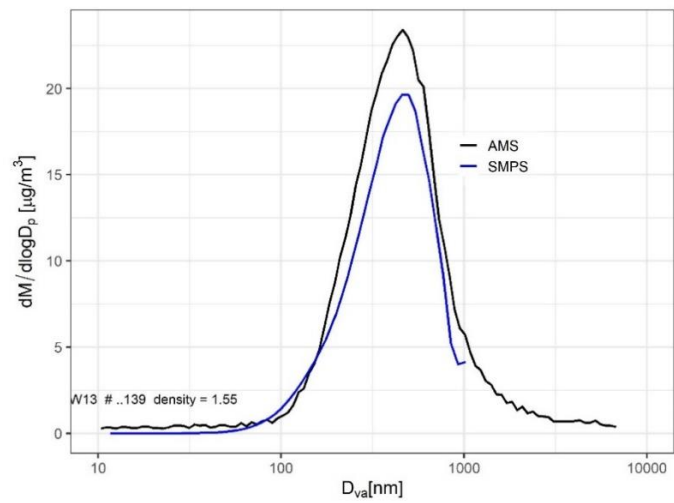
1006



1007



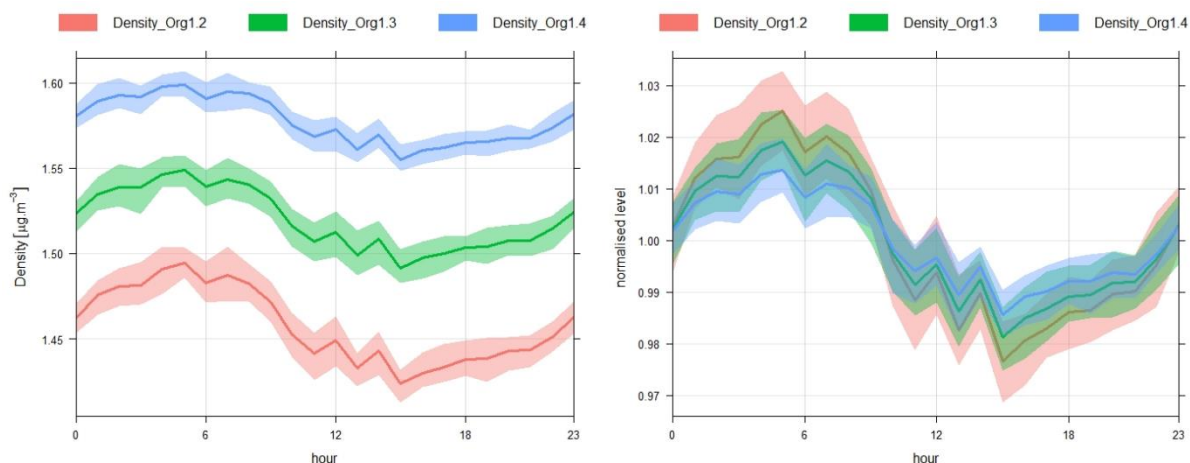
1008



1009

1010 Figure A10. Fit of AMS and MPSS mass size distribution spectra of winter episodes (W1 –
 1011 W13) for density calculation.

1012



1013

1014 Fig. A11. Diurnal trends of average ρ_m calculated based on Eq. (2) in winter for different
 1015 organic densities (1.2, 1.3 and 1.4 g cm^{-3}) in absolute (left) and normalized (right) values.

1016

1017 **A1. Positive Matrix Factorization on PNSD**

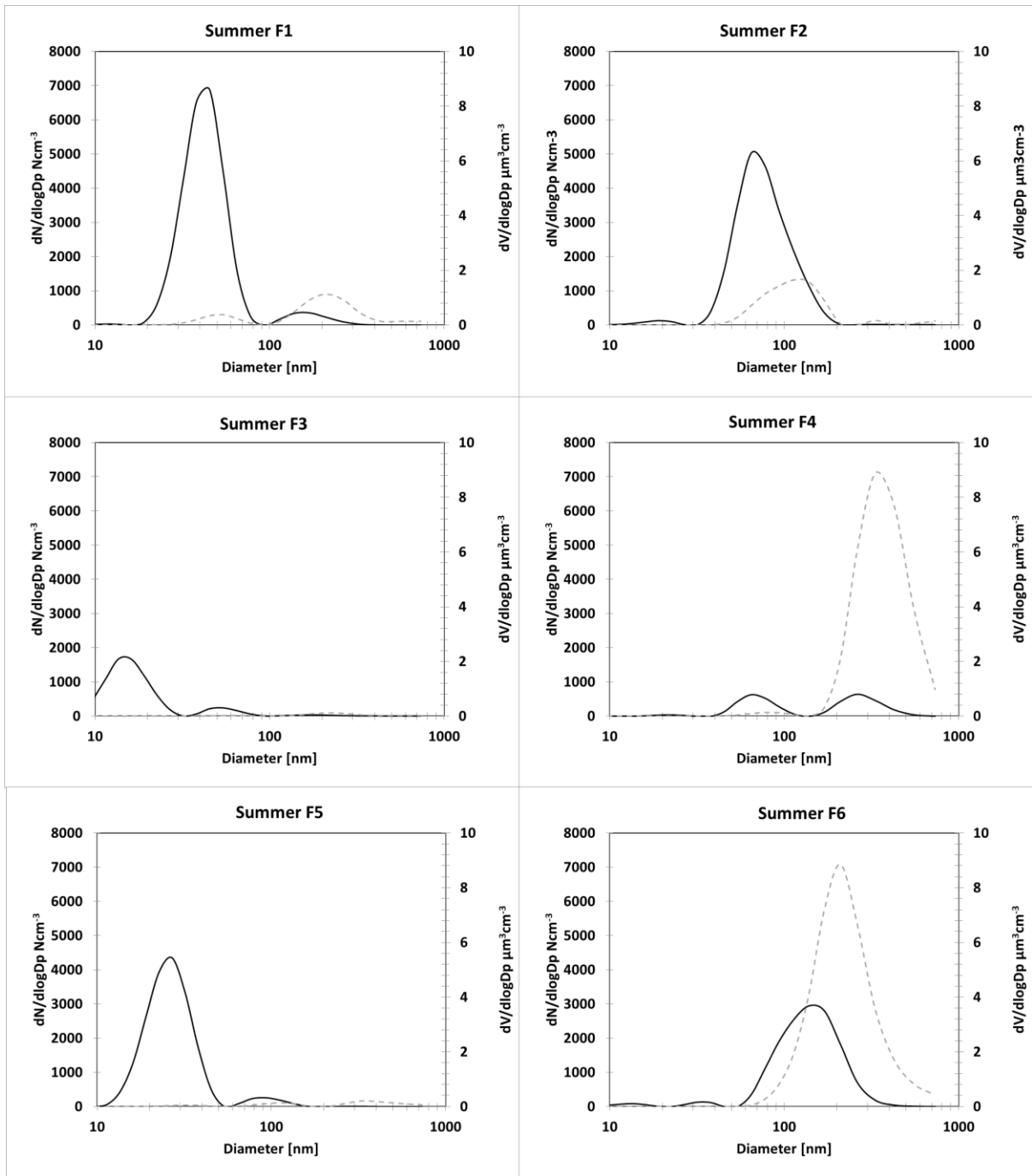
1018

1019 PMF (US EPA, version PMF 5.0) was applied to the seasonal 5-min PNSDs in the range of 10
 1020 nm to 800 nm to estimate the number and profile of the PNSD factors and their contributions
 1021 to the receptor. Application of PMF on PNSD is commonly adopted in source apportionment
 1022 studies since by investigating particles in various size ranges, it is possible to more clearly
 1023 identify and apportion contributions from those sources that contributed more to the particle
 1024 number than to the particle mass (e.g. Beddows et al., 2015; Masiol et al., 2016; Sowlat et al.,
 1025 2016; Leoni et al., 2018; Pokorná et al., 2020; Zíková et al., 2020). Episodes in which the factor
 1026 contributions to the total particle number concentrations were higher than 80 % were chosen
 1027 for the subsequent particle density calculations.

1028 The input data were prepared by merging three consecutive bins to reduce the noise in the raw
 1029 data, decrease the number of variables, and reduce the number of zeroes in the raw data (Leoni
 1030 et al., 2018). The uncertainties were calculated according to Vu et al. (2015). The total variables
 1031 were calculated by summing all the bins (N10 – 800). PMF was conducted using different
 1032 uncertainty input matrices and different C3 (Vu et al., 2015) to obtain the Q_{true} closest to
 1033 Q_{expected} ; different modelling uncertainties and different numbers of factors were also applied.
 1034 A C3 of 0.8 was chosen.

1035 The PMF model was run several times until the most physically meaningful results (factor
 1036 profiles, contributions to N10-800 and origin) and the best diagnostics were obtained. The four
 1037 (9.7 nm, 11.5 nm, 557.2 nm and 733.6 nm; midpoint of the merged three consecutive size bins)
 1038 were set as weak along with the total variable (N10 – 800). The model was run with different
 1039 factor numbers (3 – 8). The most stable solution was found when 6 factors in summer and 5
 1040 factors in winter were considered (Fig. A12). With all runs converged, the scaled residuals were
 1041 normally distributed, and any unmapped factors were detected with bootstrap error estimations.
 1042 No swaps were observed with the displacement error analysis, indicating that the solution was
 1043 stable (Table A2). The non-normalized PNSD (N cm^{-3}) was analysed using the model.

1044



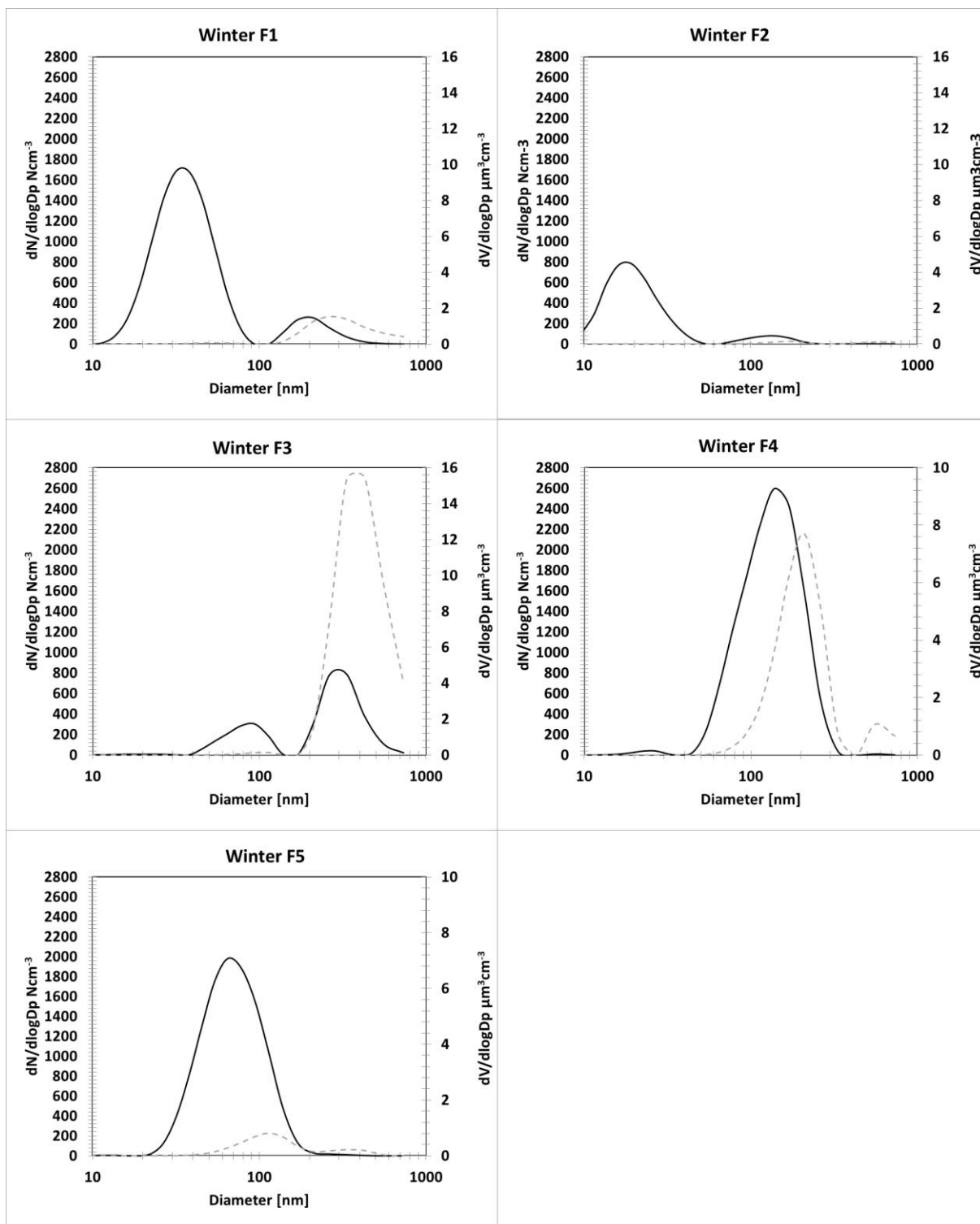
1045

1046

1047

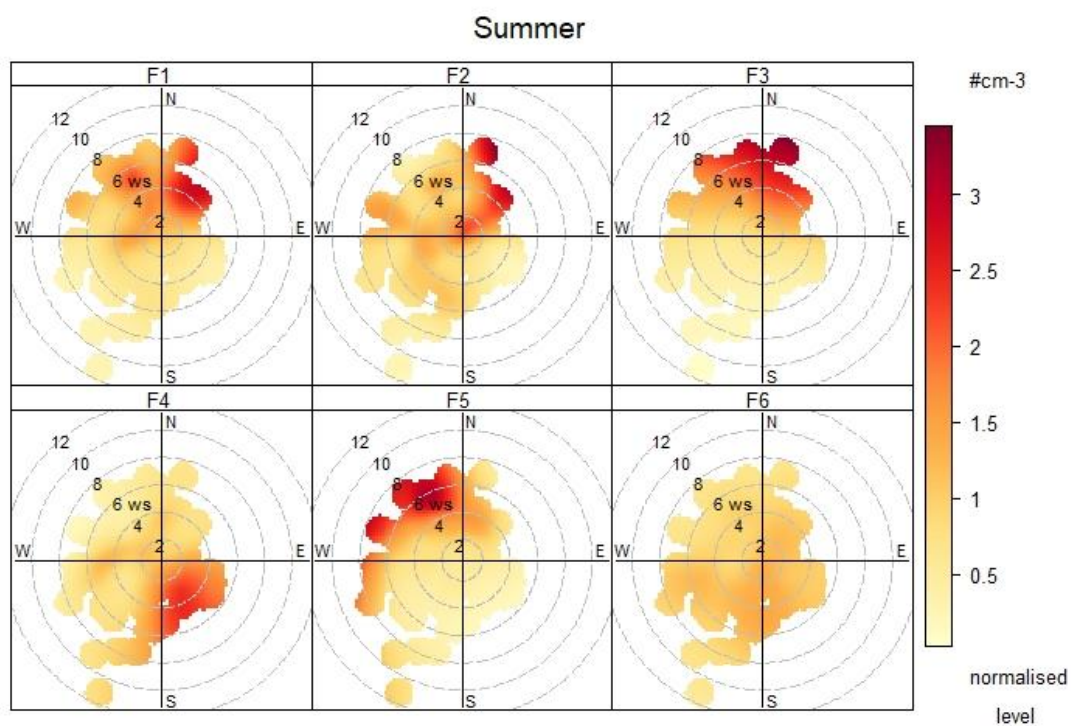
1048

1049

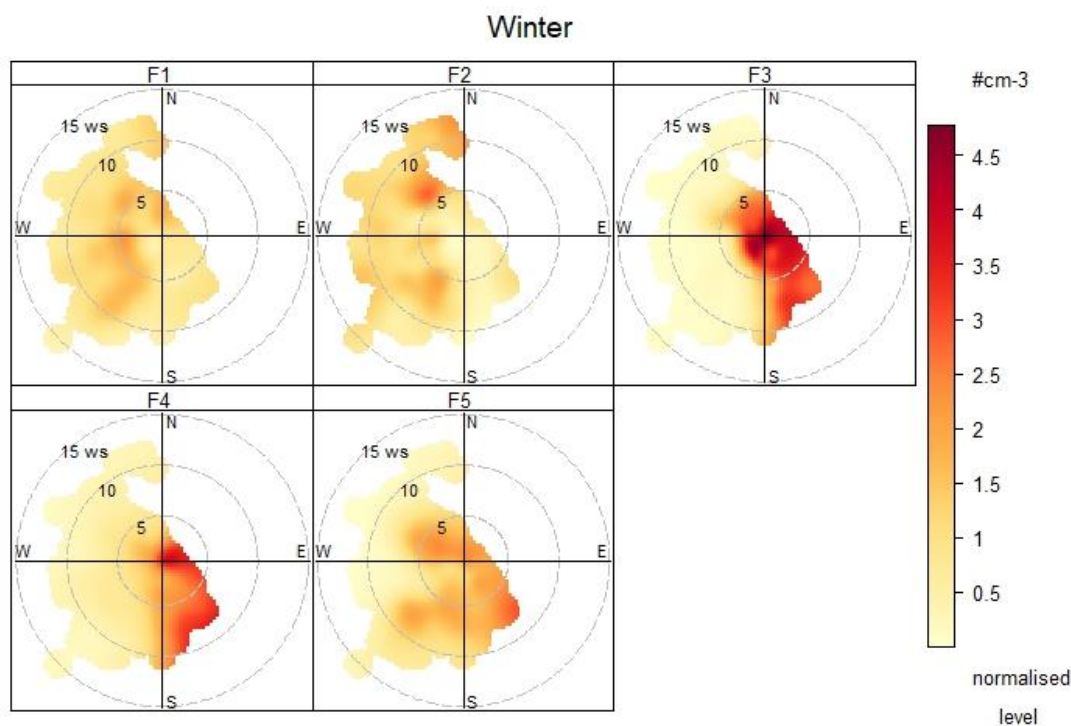


1050

1051 Figure A12. PNSD factor profiles for summer (top) and winter (bottom) campaign. NSD (black
 1052 line, y-axis on the left), volume size distribution (grey dashed line, y-axis on the right). The
 1053 volume size distribution was re-calculated from the NSD assuming spherical particles.



1054



1055

1056 Figure A13. Polar plot with factors concentrations (1-h vector averaged WS and WD) for
 1057 summer (top) and winter (bottom).

1058 Table A2. Summary of PMF diagnostics for PNSD.

Diagnostic	Summer	Winter
N. of observations	8684	7414
Missing values	6.8%	0%
Number of factors	6	5
Q_{expected}	161224	103701
Q_{true}	129774	102925
Q_{robust}	130657	103495
Species with $Q/Q_{\text{expected}} > 2$	0	263
Extra modelling uncertainty	4.8%	4.0%
DISP swaps	0	0
BS mapping	100%	100%

1059

1060

1061 Table A3. Overview table presenting median diameter (d) of N10-800 calculated by fitting log-
 1062 normal function to the MPSS size distributions for the selected episodes (N_W1 – N_W8) along
 1063 with meteorology recorded during the episodes (relative humidity – RH, global radiation – GR,
 1064 temperature – T, wind speed – WS and wind direction – WD)

Episode	Start	End	Duration [min]	$d_{\text{N10-800}}$ [nm]	RH [%]	GR [W m ⁻²]	T [°C]	WS [m s ⁻¹]	WD [°]
N_W1	1.22.20 3:00	1.22.20 4:00	60	623	96.6	0	-5.8	2.2	SE
N_W2	1.28.20 23:35	1.29.20 00:10	35	265	74.2	0	1.3	7.1	SW
N_W3	1.29.20 00:30	1.29.20 01:05	35	283	83.6	0	0.2	7.1	SW
N_W4	1.29.20 07:25	1.29.20 08:55	90	300	82.3	10	-0.4	6.0	S
N_W5	1.30.20 01:30	1.30.20 02:00	30	269	81.3	0	0.3	7.6	W
N_W6	1.30.20 05:35	1.30.20 05:55	20	356	84.0	0	-0.2	5.7	SW
N_W7	2.2.20 19:00	2.2.20 19:30	30	261	90.8	0	9.0	8.8	SW-W
N_W8	2.5.20 00:40	2.5.20 01:15	35	358	95.2	0	-0.1	8.3	W

1065

1066 References

1067

1068 Beddows, D.C.S., Harrison, R.M., Green, D.C, Fuller, G.W., 2015. Receptor modelling of both
 1069 particle composition and size distribution from a background site in London, UK. *Atmos.*
 1070 *Chem. and Phys.* 15, 10107-10125.

1071 Leoni, C., Pokorná, P., Hovorka, J., Masiol, M., Topinka, J., Zhao, Y., Křůmal, K., Cliff, S.,
 1072 Mikuška, P., Hopke, P.K., 2018. Source apportionment of number size distributions and
 1073 mass chemical composition in a European air pollution hot spot. *Environmental Pollution*
 1074 234, 145-154.

- 1075 Masiol, M., Vu, T. V., Beddows D. C. S., Harrison R. M., 2016. Source apportionment of wide
1076 range particle size spectra and black carbon collected at the airport of Venice (Italy). *Atmos.*
1077 *Environ.* 139, 56-74.
- 1078 Pokorná, P., Leoni, C., Schwarz, J., Ondráček, J., Ondráčková, L., Vodička, P., Zíková, N.,
1079 Moravec, P., Bendl, J., Klán, M., Hovorka, J., Zhao, Y., Cliff, S.S., Ždímal, V., Hopke, P.K.,
1080 2020. Spatial-temporal variability of aerosol sources based on chemical composition and
1081 particle number size distributions in an urban settlement influenced by metallurgical
1082 industry. *Environmental Science and Pollution Research* 27, 38631–38643.
- 1083 Sowlat, M H., Hasheminassab S., Sioutas C., 2016. Source apportionment of ambient particle
1084 number concentrations in central Los Angeles using positive matrix factorization (PMF).
1085 *Atmos. Chem. Phys* 16, 4849-4866.
- 1086 Zíková, N., Pokorná, P., Makeš, O., Sedlák, P., Pešice, P., Ždímal, V., 2020. Activation of
1087 atmospheric aerosol in fog and low clouds. *Atmospheric Environment* 230, 117490, 1–11.